143 (2025) 205726

Contents lists available at ScienceDirect

Gas Science and Engineering

journal homepage: www.journals.elsevier.com/gas-science-and-engineering

Time-dependent deformation and permeability evolution in porous sandstones: Implications for underground hydrogen storage

Ming Wen [a,*], Qianyou Wang [b], Nick Harpers [a,d], Nathaniel Forbes Inskip [a], Jim Buckman [c], Kamaljit Singh [c], Paul Miller [a], Andreas Busch [a]

[a] The Lyell Centre, Heriot-Watt University, UK, Edinburgh, EH14 4AS, UK
[b] Department of Earth, Ocean and Ecological Sciences, University of Liverpool, Liverpool, L69, UK
[c] Institute of GeoEnergy Engineering, Heriot-Watt University, UK, Edinburgh, EH14 4AS, UK
[d] Applied Structural Geology Teaching and Research Unit, RWTH Aachen University, 52064, Aachen, Germany

ARTICLE INFO

Keywords:
Underground hydrogen storage
Porous sandstone
Time-dependent deformation
Porosity
Permeability
Microstructural analysis
Burgers model

ABSTRACT

During underground hydrogen storage (UHS) operations, reservoir rocks often experience time-dependent deformation under long-term stress, which can alter the microstructure and subsequently affect the stability and hydrogen storage efficiency. Therefore, understanding and predicting these time-dependent deformation of reservoir rocks under *in situ* conditions and its impact on rock properties are crucial for ensuring the long-term safe operations of UHS. This study investigates the time-dependent mechanical and transport behaviour of three representative porous sandstones—St Bees, Castlegate, and Zigong—through constant stress (creep) and multi-level stress creep experiments. These tests were designed to simulate the *in situ* conditions (1.3–2.6 km depth) of the underground hydrogen storage process at a laboratory scale. In the constant stress experiments, permeability and porosity were measured concurrently to reveal the impact of time-dependent deformation on the transport properties of porous sandstones. In the multi-level stress creep tests, long-term pore pressure cycling was applied to simulate hydrogen injection and withdrawal, and the results were compared with those from experiments under constant pore pressure. This allowed for a systematic assessment of the influence of pore pressure fluctuations on the mechanical response and transport characteristics of the sandstones. The research results indicate that all three sandstones exhibit stable creep behaviour, with the steady-state creep rate increasing as temperature and stress increased. The high-porosity St Bees and Castlegate Sandstones show higher steady-state creep rates under the same conditions compared to the low-porosity Zigong Sandstone. The creep behaviours of the three sandstones under *in situ* conditions can be well described by Burgers model. The permeability of the three sandstones gradually decreased during the experiments, and this trend become more obvious as the stress and temperature increases. Microstructural analysis reveals that the deformation mechanism of the high-porosity St Bees Sandstone is dominated by dilatancy. Although shear-induced deformation causes the feldspar and quartz clusters to fracture, creating new voids and increasing the overall porosity, the fractured debris from these clusters block the throats, complicating the pore structure and leading to a significant permeability loss. The deformation mechanisms of Castlegate and Zigong Sandstone, on the other hand, are dominated by compaction, with pore compression and microcrack closure being the primary causes of porosity, permeability losses. Pore pressure cycling increases the creep rate of sandstones, accumulating more inelastic strain especially in St Bees Sandstone, but has limited effect on the properties of Castlegate and Zigong Sandstones.

1. Introduction

The global energy landscape is transforming alongside an ever-growing demand for clean energy. Hydrogen has been identified as a potentially clean source of energy and is therefore receiving increasing attention worldwide due to its potential to a mitigate the intermittency

---

This article is part of a special issue entitled: Underground H2 Storage published in Gas Science and Engineering.

* Corresponding author.

E-mail address: mw107@hw.ac.uk (M. Wen).

https://doi.org/10.1016/j.jgsce.2025.205726
Received 11 December 2024; Received in revised form 4 July 2025; Accepted 7 July 2025

of renewable energy sources. It can provide long-term energy storage solutions, which are significant for facilitating the transition to renewable energy and reducing carbon emissions (McPherson et al., 2018; Zivar et al., 2021). When demand for hydrogen is locally low, but the generating potential from renewable energy is high, there is a need for temporarily storing hydrogen (Lankof and Tarkowski, 2020; Muhammed et al., 2022). The geological subsurface has been identified as a suitable target. As such, similar to underground natural gas storage, underground hydrogen storage (UHS) involves injecting hydrogen into reservoir rocks, such as porous sandstone, for future use (Heinemann et al., 2021). However, in practical applications, UHS faces numerous challenges; one of which is the mechanical response of reservoir rocks during long-term hydrogen storage and its impact on storage capacity (Heinemann et al., 2021; Kumar et al., 2023; Reitenbach et al., 2015). Reservoir rocks often exhibit creep behaviour under *in situ* stress conditions, which refers to the slow and continuous deformation of rocks under constant stress conditions (Brantut et al., 2012, 2013). This time-dependent deformation not only affects the mechanical properties of reservoir rocks but also changes its internal pore structure and permeability (Brzesowsky et al., 2014; Hangx et al., 2010; Wang and Hao, 2023; Wu and Liu, 2022), thus adversely affecting storage capacity and injection/extraction efficiency of hydrogen in the reservoir rocks. Therefore, conducting in-depth research on the time-dependent deformation of reservoir rocks and its impact on transport properties can help to better understand and predict reservoir performance under long-term hydrogen storage conditions. This is crucial for ensuring reservoir stability and safety, optimizing the UHS process, and developing appropriate operational strategies.

Despite numerous studies on the creep behaviour of reservoir rocks, most of them have limitations when applied to UHS. For example, the stress and temperature conditions used in previous research cannot accurately reflect the *in situ* stress and temperature states experienced by UHS reservoirs located in shallow (<5 km) crustal layers (Iglauer, 2022; Muhammed et al., 2022), leading to significant discrepancies between experimental results and real-world scenarios (Chu et al., 2022; Liu et al., 2016; Sabitova et al., 2021; Yang and Hu, 2018). Moreover, many studies primarily focused on the mechanical response of reservoir rocks during creep process, neglecting the time-dependent effects of on rock transport properties. These studies typically emphasized stress-strain relationships, creep models, and creep failure mechanisms, providing insights into the macroscopic mechanical behaviour of reservoir rocks during creep (Chu et al., 2022; Sabitova et al., 2021; Wu et al., 2020; Wu and Liu, 2022; Zhang et al., 2016). In contrast, there is relatively little research on the changes in transport properties of reservoir rocks during creep, especially from a microscopic perspective (Chu et al., 2021, 2022). Therefore, our understanding of the coupled behaviour between creep and permeability in reservoir rocks, as well as the impact of pore pressure remains limited. Specifically, pore pressure oscillations caused by gas injection and withdrawal can significantly affect reservoir rock properties, potentially leading to geological risks such as surface subsidence and fault reactivation (Asahina et al., 2019; Liu et al., 2019; Noël et al., 2019, 2021; Raziperchikolaee et al., 2022; Zhong et al., 2021). These research limitations prevent our comprehensive and in-depth understanding and predicted reservoir rocks properties in UHS.

To overcome the limitations of previous studies and gain a more comprehensive understanding of the creep behaviour of reservoir rocks and expected impact on transport properties in UHS, this study is making use of three different porous sandstones for creep (constant stress) experiments to simulate *in situ* conditions. Permeability and porosity were measured simultaneously during constant stress experiments to investigate the effects of time-dependent deformation on the transport properties of porous sandstones. In addition, pore pressure oscillation tests were conducted to simulate cyclic pore pressure variations characteristic of underground hydrogen storage (UHS). To further reveal the microstructural mechanisms underlying the observed changes in rock properties, scanning electron microscopy (SEM) and X-ray micro-computed tomography (micro-CT) were employed to characterize the internal structure of sandstone samples after the experiments. A comprehensive analysis of both macroscopic experimental data and microstructural observations provides insight into the mechanisms governing creep behaviour and their impact on mechanical and transport properties. The findings aim to provide foundational insights for assessing safety and efficiency in UHS and subsurface gas storage systems.

2. Materials and methods

2.1. Sample description and preparation

In this study, relatively homogeneous, quartz-rich sandstones—St Bees, Castlegate, and Zigong—were selected to isolate mechanical processes and minimise the influence of chemical reactions. All samples were obtained from local outcrops. Castlegate (CG) is a yellow sandstone from the upper Cretaceous Mesaverde Group. It is primarily composed of quartz (~65 %–90 %), feldspar (~20–30 %) and rock fragments (~10–20 %). The grain size generally ranges from medium to coarse, with an average particle diameter of ~0.25 mm. It exhibits good sorting, high roundness, and strong homogeneity (Miall and Arush, 2001). CG Sandstone typical has high porosity and high permeability, making it an excellent reservoir rock, often regarded as the ideal analogue for experimental reservoir studies (Kibikas and Bauer, 2021; Mortazavi and Atapour, 2018). The porosity ranges from 20 to 30 %, primarily consisting of intergranular pores. The permeability often exceeds several hundred millidarcies (mD). St Bees (ST) is a Permian red sandstone primarily distributed in Cumbria, England. Quartz is the predominant component (~70–90 %), followed by feldspar (K-feldspar and plagioclase, ~10–20 %) (Hawkins and McConnell, 1991). Additionally, this sandstone contains minor amounts of rock fragments and hematite, the latter giving it its red colour. The grain size of ST sandstone typically ranges from fine to medium, with an average diameter of ~0.15 mm, exhibiting favourable sorting and sub-angular to sub-rounded shapes. ST Sandstone has good porosity (10–25 %) and good permeability (up to several hundred mD). This sandstone is considered an important aquifer reservoir rock. Finally, Zigong (ZG) Sandstone is primarily found in the Sichuan Basin, China. It is mainly composed of quartz (30–60 %) and feldspar (up to 60 %). The average grain size is ~0.25–0.3 mm, similar to that of CG sandstone (Zhang et al., 2020). The grains are well-rounded or sub-rounded and well-sorted. Compared to the other two types of sandstone, ZG Sandstone exhibits lower porosity of <10 % and permeability of few mD. It is typically used in laboratory-scale studies to simulate low-permeability reservoir rocks.

Prior to testing, cylindrical samples with a diameter of 9–10 mm and a length of 19–21 mm were drilled perpendicular to bedding and the ends were polished with sandpapers for equal length of ≤0.05 mm, ensuring even load distribution during the testing process. After preparation, the samples were dried in an oven at 70 °C for 48 h, and the dimensions and mass of the samples were measured. The mechanical properties of the sandstone samples were measured using an MTS815 rock mechanics servo-controlled testing system through uniaxial compression tests. Young's Modulus was determined by calculating the slope of the stress-strain curve in the linear phase. Additionally, the porosity was tested by conducting micro-CT scans on the samples before the experiments and calculated using the digital rock method. The basic physical properties of the sandstone selected for this study are shown in Table 1.

2.2. Experimental methods

The depth selection for UHS is an important aspect, as it directly affects the safety, cost, and efficiency of the UHS process. When too shallow, it may lead to inadequate sealing and subsequent environmental concerns, when too deep costs and operational complexities can

Table 1
Physical properties of the porous sandstone samples.

Rock Type	CG Sandstone	ST Sandstone	ZG Sandstone
Porosity (%)[a]	18.8	20.1	10.2
UCS (MPa)[b]	65	52	89
Young's Modulus (GPa)	5.24	4.25	12.21
Poisson's ratio (υ)	0.23	0.21	0.30

Note: *a* Porosity is calculated using grayscale differences after Micro-CT scanning the whole rocks.
b Uniaxial compressive strength (UCS) refers to the maximum pressure that sandstone can withstand during a uniaxial compression test.

significantly increase. Previous research indicates that the optimal depth for UHS ranges from 1100 to 1600 m, while depths exceeding 3700 m are theoretically unsuitable for long-term, large-scale UHS (Iglauer, 2022; Muhammed et al., 2022). Accordingly, creep experiments were conducted under stress and temperature conditions representative of depths ranging from approximately 1.3 to 2.6 km.

2.2.1. *Experimental apparatus*

The constant pressure experiment and permeability test were performed using the Harpers THMC Flow Bench, as shown in Fig. 1. This system was designed to replicate *in situ* stress and temperature conditions for coupled thermo-hydro-mechanical-chemical experiments on rock samples with diameters of 1 × 2 cm. The experimental setup consists of four identical high-pressure cells, which can operate concurrently under the same experimental conditions. Axial load is provided through high pressure nitrogen and controlled by a spindle pump. The gas pressurises an axial load intensifier that amplifies the provided gas pressure by a factor of 15. Two high pressure syringe pumps are responsible for supporting the system with confining pressure (Teledyne ISCO Model 260D, USA)) and pore pressure (Teledyne ISCO Model 500D, USA), respectively.

2.2.2. *Constant (creep) stress tests with permeability tests*

In this study, the maximum *in situ* stress (σ_1) was assumed to act in the vertical direction, with its magnitude estimated as the integral of rock density from the surface to the target depth z (Zoback, 2010):

$$\sigma_1 = \int_0^z \rho(z) g dz \approx \overline{\rho} g z \tag{1}$$

The sandstone's bulk density $\overline{\rho}$ is approximately 2.3 g/cm^3 (Fjaer et al., 2008; Tiab and Donaldson, 2024). The experimental design includes three levels of axial stress - 30, 45 and 60 MPa - simulating the *in situ* stress conditions at depths of 1304 m, 1956 m, and 2608 m, respectively. During the experiment, sandstone samples were wrapped with PTFE (polytetrafluoroethylene) tape to prevent fluid leakage through the gaps between the sandstone and the inner walls of the core holders. The wrapped samples were then placed inside the core holders, which were subsequently installed in the high-pressure cells and vacuumed for 15 min. Following this, a high-pressure syringe pump (Teledyne ISCO Model 260D, USA) was used to inject deionised water into the samples at a constant rate of 0.5 ml/s, applying confining pressure until the predetermined value of 11 MPa was reached. Simultaneously, axial stress was applied using a spindle pump to match the confining pressure, thereby maintaining a hydrostatic state. Once both the confining pressure and axial stress were stabilised, a syringe pump (Teledyne ISCO Model 500D, USA) was used to gradually introduce deionised water into the core holders until the pore pressure reached 6 MPa. After a 10-min equilibration period, axial stress was increased at an average rate of 0.1 MPa/s until the target value was achieved. After experiments, the samples were unloaded, removed from the core rack, dried in an oven at 70 °C for 48 h, and vertically sliced to prepare for SEM observations. Test conditions for this part are detailed in Table 2.

2.2.3. *Multi-level stress creep experiments with permeability tests*

In this study, multi-level stress creep experiments were conducted to replicate the *in situ* stress and temperature conditions at varying depths. The experimental stress path is shown in Fig. 2. Here, samples were sequentially subjected to three axial stress levels: 30 MPa, 45 MPa, and 60 MPa (Fig. 2a). These stress levels correspond to *in situ* stress conditions of 1304 m, 1956 m, and 2608 m depth, respectively. Assuming a geothermal gradient of 30 °C/km (Fossen, 2016; Zoback, 2010), the temperatures at these depths are estimated to be 49 °C, 69 °C, and 88 °C, respectively, assuming a surface temperature of 10 °C. In this study, a high-pressure syringe pump (Teledyne ISCO Model 260D, USA) was used to inject deionised water at a constant rate of 0.5 ml/s to apply confining pressure to the sample until it reached the predetermined value of 11 MPa. Subsequently, the axial pressure was increased to match the confining pressure, maintaining hydrostatic pressure on the samples. Once the confining and axial pressures stabilised, deionised water was gradually introduced into the core holders using a syringe pump (Teledyne ISCO Model 500D, USA) until the pore pressure reached a stable value of 6 MPa. Following a 10-min equilibrium period, axial pressure loading commenced at an average rate of 0.5 MPa/s until the axial pressure increased to 30 MPa. The heater was activated, and the high-pressure cells were wrapped in heat-insulating jackets to

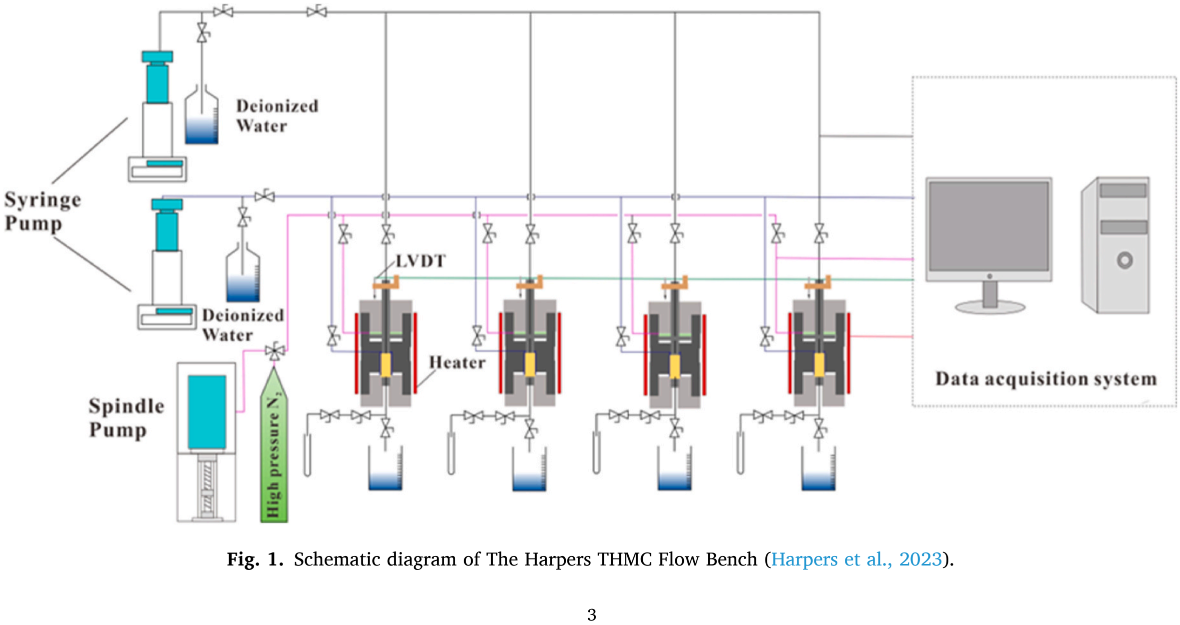

Fig. 1. Schematic diagram of The Harpers THMC Flow Bench (Harpers et al., 2023).

Table 2

Test conditions for porous sandstones.

Constant (creep) stress tests					
No.	P_a (MPa)	P_c (MPa)	P_p (MPa)	T (°C)	Duration (h)
ST-1	30	11	6	RT [a]	99.48
ST-2	45	11	6	RT	99.77
ST-3	60	11	6	RT	98.56
CG-1	30	11	6	RT	97.04
CG-2	45	11	6	RT	99.75
CG-3	60	11	6	RT	99.73
ZG-1	30	11	6	RT	99.49
ZG-2	45	11	6	RT	98.90
ZG-3	60	11	6	RT	100.10
Multi-level Creep experiments[b]					
ST-4	30–60	11	6	49–88	330.58
ST-5	30–60	11	3–9[c]	49–88	331.10
CG-4	30–60	11	6	49–88	334.90
CG-5	30–60	11	3–9	49–88	334.25
ZG-4	30–60	11	6	49–88	337.26
ZG-5	30–60	11	3–9	49–88	344.45

Note: P_a, P_c. and P_p is axial pressure, confining pressure and pore pressure respectively. a. RT is the Room temperature. b. In the multi-level creep experiments, the axial stress and temperature are divided into three stages: 30 MPa at 49°C, 45 MPa at 69°C, and 60 MPa at 88°C, to simulate the *in situ* stress and temperature conditions at different depths. c. For the samples used in the pore pressure cycling experiment, the pore pressure cycles between 3 MPa and 9 MPa to simulate gas injection and extraction conditions.

minimise the impact of the environment on the system temperature. After the temperature stabilised at 49 °C, both temperature and pressure were maintained for ~100 h while permeability changes were measured during the creep tests. Subsequently, keeping the confining and pore pressures constant, the axial pressure was increased to 45 MPa, and the temperature was raised to 69 °C, initiating the second stress level phase. During this phase, permeability changes continued to be measured. Similarly, after completing the second stress level phase, the confining and pore pressures were maintained constant, and the axial pressure was further increased to 60 MPa, and temperature increased to 88 °C, marking the beginning of the third stress level phase, after which the samples were unloaded, cooled and removed from the core holders. They were then dried and subjected to micro-CT scanning for further analysis of microstructural changes.

In UHS, reservoir rocks frequently experience cyclic pore pressure fluctuations due to annual or more frequent gas injection and extraction cycles. To investigate the response of porous rocks to pore pressure oscillations under *in situ* conditions, creep tests were performed under oscillating pore fluid pressure conditions. These tests were carried out under the same axial and confining pressures as well as temperature conditions as the multi-level creep experiments. During the creep phase, the axial stress and confining pressure remained constant. A high-pressure syringe pump (Teledyne ISCO Model 500D, USA) was used to control flow into/out of the core holders at a rate of 0.01 ml/s, causing the pore fluid pressure to fluctuate in an approximate sawtooth pattern within a range of 3–9 MPa. Each cycle of pore pressure lasted approximately 20 min, with an oscillation period comprising 10 cycles (Fig. 2b). The decision to perform 10 cycles was made to balance the practical limitations of experimental duration with the need to ensure sufficient repeatability to capture the key trends in mechanical behaviour and permeability evolution. Upon completion of the pore pressure oscillations, the system pore pressure was stabilised at 6 MPa, and the permeability of the porous sandstone was measured. After the experiments, the samples were removed, dried, and subjected to micro-CT scanning. See Table 2 for details of the samples and experimental conditions for the multi-level stress creep tests.

2.3. Microstructural characterization

2.3.1. SEM observations

After creep experiments, samples were cut in slabbed along the axis

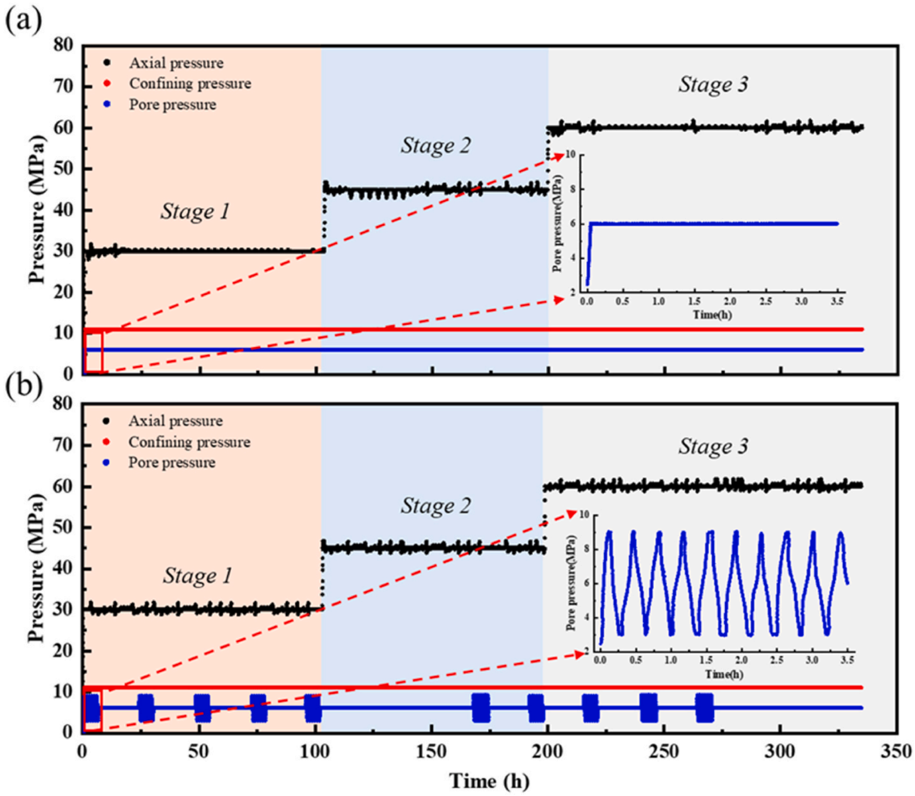

Fig. 2. Schematic diagram of experimental stress paths. (a) Creep experiments at constant pore pressure. (b) Creep experiments under pore pressure oscillations.

and placed in mounting cups of a 2 cm radius. EpoFix Resin and EpoFix Hardener were added to the containers in a 25:3 mass ratio, stirred for 1 min with a stirrer to remove air bubbles from the resin and placed in a vacuum pump under vacuum at 0.17 Bar for 15 min, then removed and left to dry for more at least 24 h. After the samples had dried, the cut surfaces were initially polished with a Saphir 330-wheel grinder and then polished with a LaboForce-100 machine using a water based diamond suspension at 150 rpm for 30 min to obtain a precision polished surface. The polished surfaces were carbon coated and observed with a Zeiss GeminiSEM 450. Pore and fracture development were observed using SE2 mode and BSE mode with an accelerating voltage of 20 kV, a current of 1 nA and a working distance of 10 mm (Wang et al., 2025; Wang et al., 2023).

2.3.2. *X-ray Micro-CT scanning*

X-ray micro-CT scans were performed on cylindrical samples before and after multi-level creep experiments to characterize microstructural changes. It should be noted that in this study, the samples scanned before the experiments are twin samples. All CT experiments were conducted using an EASYTOM μCT scanning device manufactured by RX-Solutions (France). The scanner operates at a voltage of 100 kV and a current of 9.6 μA. Each scan took between 120 and 150 min and generated projection images with a voxel size ranging from 6 to 8 μm. Subsequently, these projection images were reconstructed into three-dimensional images using RX-Solutions analysis software, resulting in 3900–4400 2D slices. After reconstruction, the 2D slices generated were processed and analysed using Avizo 2020 (Thermo Fisher scientific Co., USA). Denoising was performed using the non-local means and median filtering method. Subsequently, the optimal threshold for pore segmentation was determined using the watershed algorithm. Upon the completion of pore segmentation, a logical algorithm was used to further segment the sandstone particles. After the segmentation, connected pores were processed and pore network models (PNMs) were constructed using the maximal ball algorithm to investigate the microscopic mechanisms governing changes in transport properties. (Dong and Blunt, 2009). The 3D reconstructions of ST, CG, ZG and corresponding pore network models (PNM) are illustrated in Fig. 3.

2.4. *Data treatment and analysis*

In data processing, the geomechanical convention was adopted, whereby compressive stresses and strains are defined as positive. (Fossen, 2016). In this study, the LVDTs (Linear Variable Differential Transformer; range ±1 mm; accuracy ±1 μm, RDP Electronics Ltd, UK) record the displacement signal of the pistons in real time. After appropriate corrections, the total axial strain ε_t was obtained:

$$\varepsilon_t \approx \frac{\Delta L}{L_0} \tag{2}$$

where ΔL represents the change in sample length, and L_0 is the initial sample length. The steady-state strain rate $\dot{\varepsilon}_{cr}$ for samples during creep experiments is calculated as the average axial strain rate from the onset of the steady-state creep phase up to just before the end of the creep experiment.

Permeability was measured by connecting the downstream end of the sample to the atmosphere while maintaining a constant pore pres-

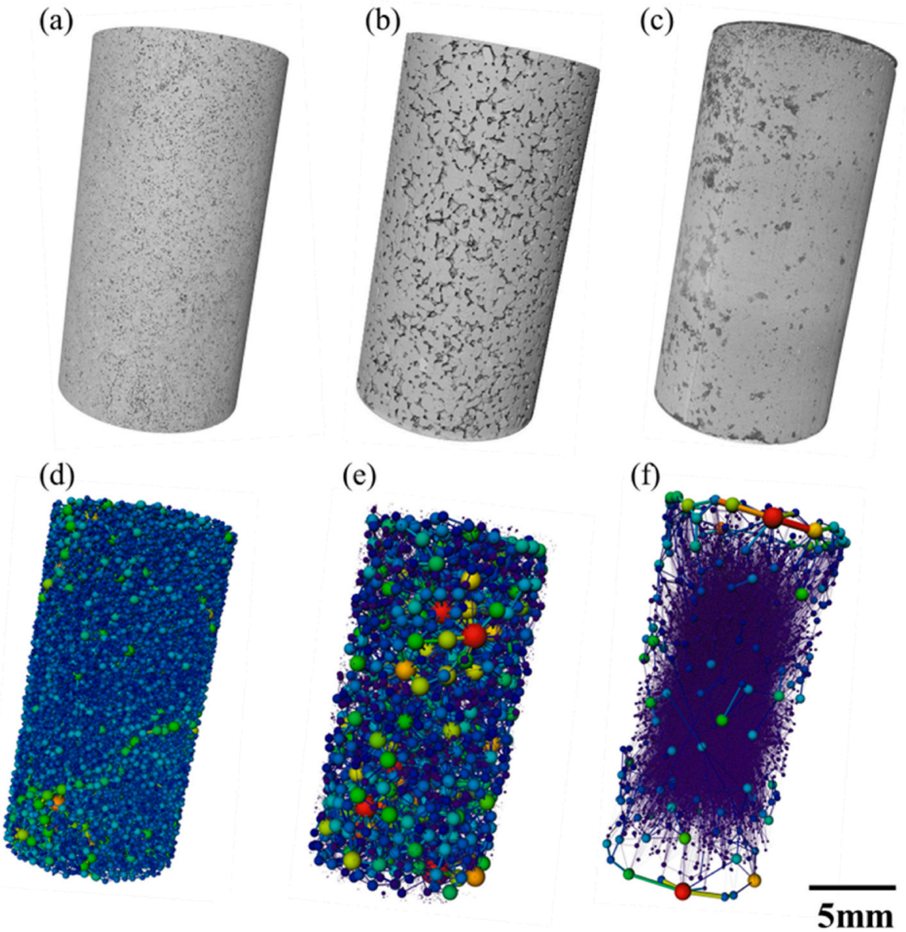

Fig. 3. 3D reconstruction and pore network models (PNM). (a), (b), (c) are the 3D reconstructions of ST, CG, and ZG Sandstones. (d), (e), (f) are the corresponding pore network models (PNM).

sure at the upstream end, thereby generating a pressure gradient that enabled deionised water to flow through the sample. Once a steady-state flow rate was achieved, the permeability was calculated using Darcy's law (Brice and Levin, 1962; Darcy, 1856):

$$k = \frac{q\mu L}{\Delta p A} \tag{3}$$

where q, μ, Δp are the fluid velocity ($m^3.s^{-1}$), viscosity (Pa.s), and the pore pressure drop between the upstream and downstream the sample (Pa), respectively, and A and L are the sample cross-sectional area (m^2) and length (m), respectively.

In this study, the porosity of porous sandstone was determined through the analysis of scanning electron microscopy (SEM) and Micro-CT images. A median filter was initially applied to minimise noise interference during pore extraction. Subsequently, interactive and top-hat thresholding was utilised to extract pore distribution data from two-dimensional images. The extracted pore areas were then compared to the total image area to calculate the 2D porosity. In addition, the 2D CT images were stacked to reconstruct a three-dimensional model. The 3D porosity was calculated by segmenting the pore volume within the reconstructed model and comparing it to the total sample volume. A schematic illustrating the methodology for porosity calculation based on SEM and micro-CT data is presented in Fig. 4.

3. Results

3.1. Mechanical data

Fig. 5 illustrates the evolution of axial strain with differential stress, as well as the time-dependent behaviour of axial strain and permeability for the three sandstones during the creep experiments. During the initial loading phase, with differential stress $Q < 15$ MPa, ST and CG exhibit nonlinear, concave-up stress-strain behaviour, which is attributed to the closure of pre-existing microcracks (Peng et al., 2015; Zhang and Tang, 2020). As the differential stress increases, this behaviour transitions to a nearly linear elastic trend. Within this near-linear trend, Young's Modulus (i.e., the slope of the linear segments) is ~4.4 and 6.8 GPa for ST and CG, respectively. With a further increase in differential stress, both stress-strain curves exhibit an inflection point, transitioning to a distinctly concave-down characteristic. This is observed at $Q \approx 40$ MPa in ST-3 and $Q \approx 45$ MPa in CG-3, as shown in Fig. 5a and c. In contrast, ZG predominantly exhibits near-linear elastic stress-strain behaviour during loading period, with a Young's Modulus of ~12.9 GPa. A slight concave-down stress-strain behaviour is observed in ZG-3 at $Q \approx 47$ MPa (Fig. 5e). AT the onset of creep, the high-porosity ST and CG sandstones exhibit greater creep strain than the low-porosity ZG sandstone under the same stress conditions. This disparity becomes increasingly pronounced as differential stress rises. At a differential stress of $Q = 19$ MPa, the creep strain is 0.09 % in ST-1, 0.07 % in CG-1, and 0.06 % in ZG-1. As Q increases to 49 MPa, creep strains of ST-3 and CG-3 increase to 0.24 % and 0.16 %, respectively, while ZG-3 shows a creep strain of only 0.08 %. Notably, compared to the steady-state creep strain rates at $Q = 19$ MPa and $Q = 34$ MPa, a significant increase in the steady-state creep strain rate is observed for ST and CG at $Q = 49$ MPa (Fig. 5b and d), whereas steady-state creep strain rates of ZG show little change. This may be closely related to changes in the internal structure of ST and CG under high-stress conditions. During the unloading stage, the stress-strain curves of the three sandstones do not coincide with the loading curves but instead form hysteresis loops, indicating the accumulation of inelastic strain. Under identical differential stress conditions, the high-porosity ST and CG sandstones exhibit greater inelastic axial strain compared to the low-porosity ZG sandstone. Notably, under low differential stress ($Q = 19$ MPa), the inelastic axial strain accumulated after unloading in the ST and CG Sandstones is similar, with ST-1 and CG-1 accumulating comparable 0.29 % and 0.27 % inelastic strain, respectively. As the differential stress increases to 34 MPa, ST-2 and CG-2 accumulate 0.39 % and 0.31 % inelastic strain, respectively, with ST showing slightly higher inelastic axial strain than CG after unloading. In the high differential stress stage ($Q = 49$ MPa), ST-3 exhibits an inelastic axial strain of 0.51 %, significantly higher than its counterpart, which only accumulates 0.31 % inelastic strain.

As evident from Fig. 6, the loading curves of the multistage stress

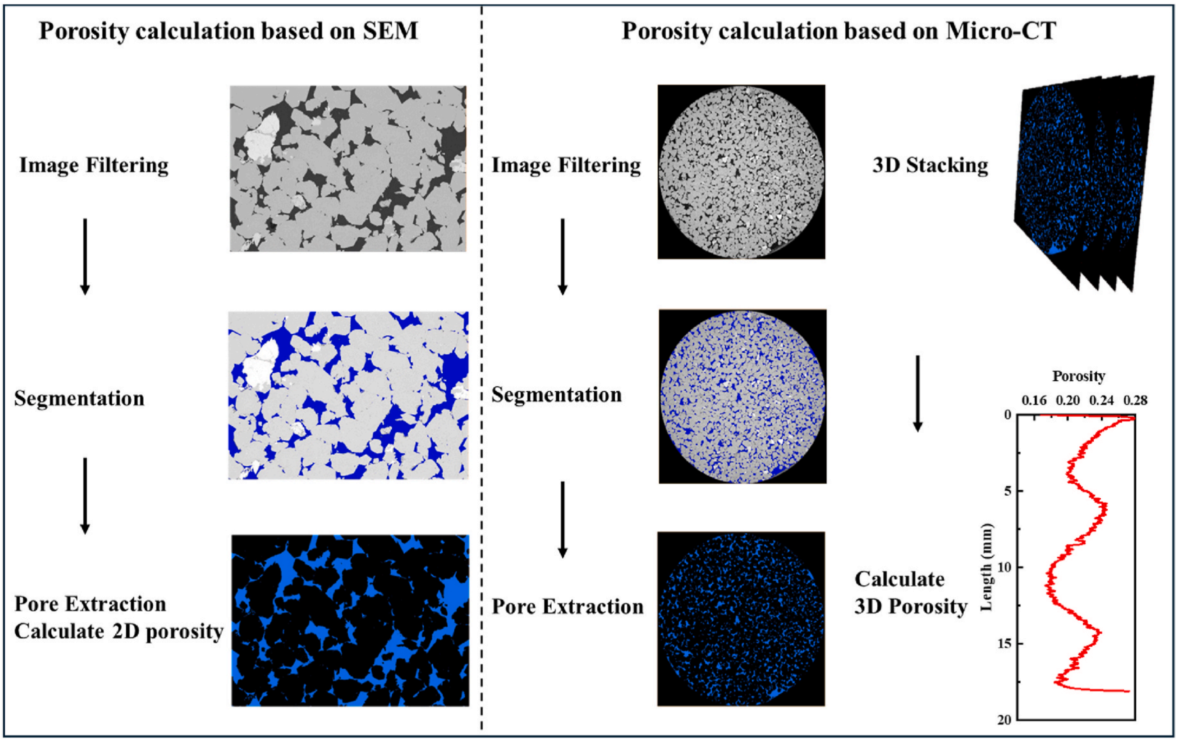

Fig. 4. Schematic diagram of porosity calculation for porous sandstone based on SEM and Micro-CT Images.

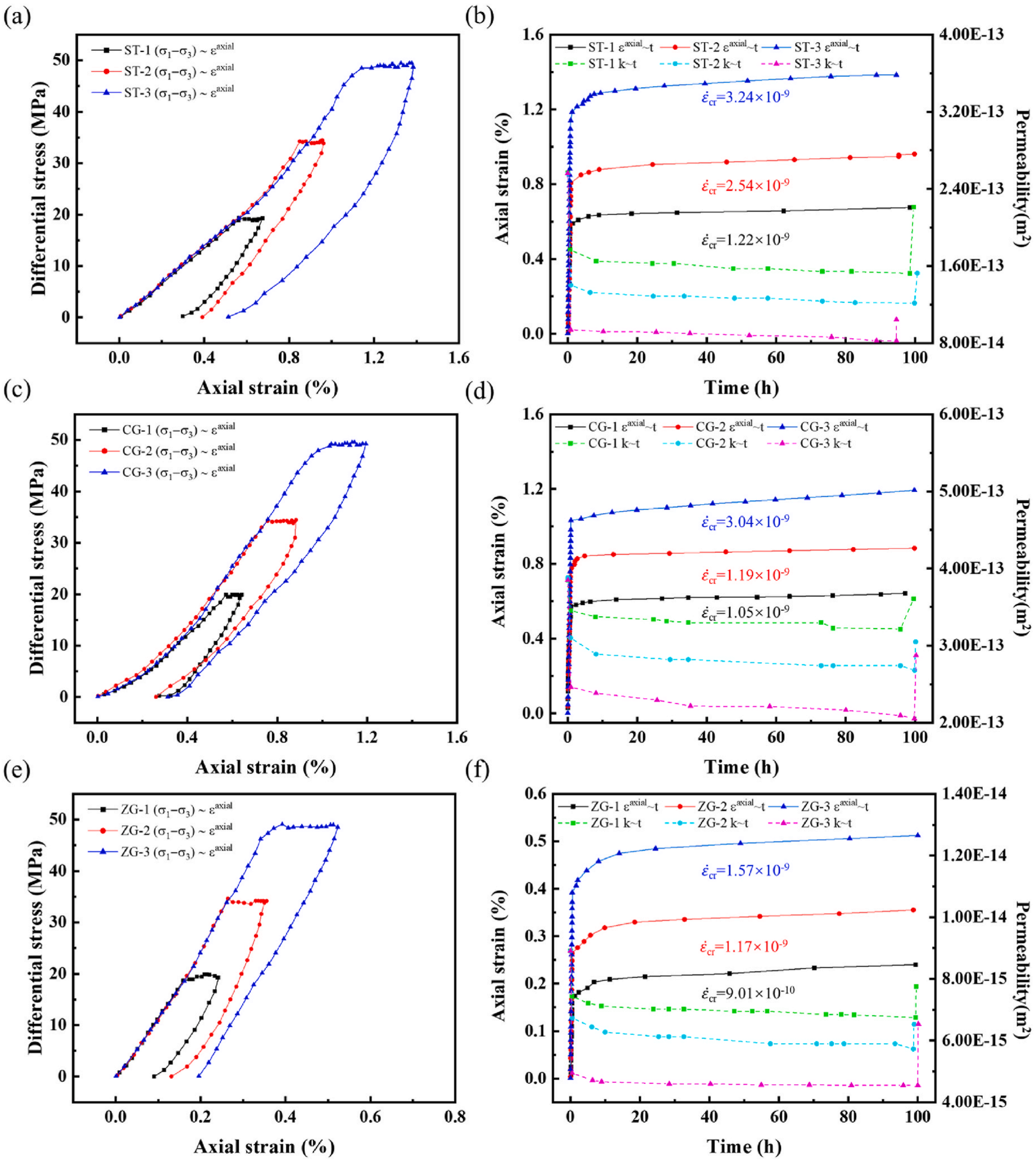

Fig. 5. Evolution of axial strain with differential stress and time-dependent characteristics of axial strain and axial permeability for the three sandstones during the creep experiments. Fig. 5a, Fig. 5c, and Fig. 5e illustrate the evolution of axial strain with differential stress for ST, CG, and ZG, respectively. Fig. 5b, Fig. 5d, and Fig. 5f illustrate the time-dependent evolution of axial strain and axial permeability for ST, CG, and ZG.

creep experiments conducted under *in situ* conditions for the three sandstones exhibit characteristics similar to those summarised in Fig. 5. Specifically, ST and CG demonstrate nonlinear, concave-up stress-strain behaviour during the initial loading stage, roughly followed by a linear elastic phase. As the differential stress further increases, the stress-strain curves of these two sandstones exhibit inflection points, displaying a pronounced concave-down characteristic. In contrast, ZG Sandstone exhibits a near linear elastic phase from the onset of loading, followed by a slight concave-down stress-strain behaviour as the stress increases. After unloading, the stress-strain curves of the three sandstones do not coincide with the loading curves, forming hysteresis loops and resulting in additional inelastic strain.

During the first creep stage ($Q = 19$ MPa), ST-4, and ST-5 exhibit a low but similar creep strains of 0.09 % and 0.10 % (Fig. 6a), with steady-state creep rates of 9.54×10^{-10} and 1.04×10^{-9}, which are slightly lower than those of ST-1 (Figs. 5b and 6b). CG-4 and CG-5 each produce again a low but similar axial strain of 0.10 % and 0.09 %, respectively, accompanied by steady-state creep rates of 1.3×10^{-9}, slightly higher than those of CG-1 (Figs. 5d and 6d). In contrast, samples ZG-4 and ZG-5 show axial strains of <0.07 % each, with a lower steady-state creep rates of 9.06×10^{-10} and 8.66×10^{-10} closely approximating those of ZG-1. (Figs. 5f and 6f). These results indicate that the influence of temperature and pore pressure cycling on sandstone creep is limited under this stage. This may be related to the relatively stable microstructure of these sandstones under low pressure and temperature conditions. In the second stage ($Q = 34$ MPa), the axial strain during the creep phase for samples ST-4 and ST-5 increased to 0.14 % and 0.15 %, with steady-state creep rates of 2.91×10^{-9} and3.11×10^{-9}, both of which are higher

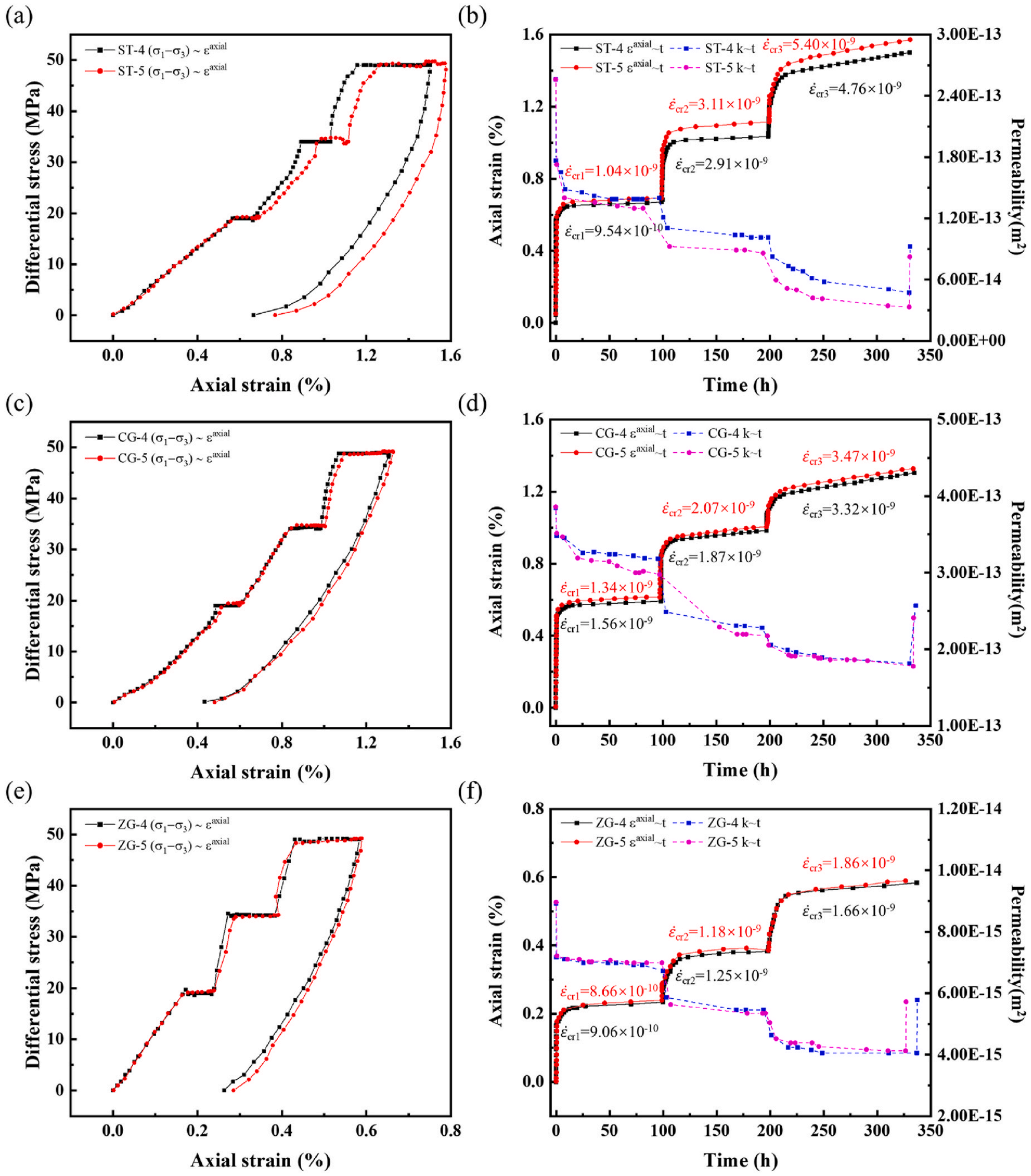

Fig. 6. Evolution of axial strain with differential stress and time-dependent characteristics of axial strain and axial permeability for the three sandstones during the multi-level stress creep experiments. Fig. 6a, Fig. 6c, and Fig. 6e illustrate the evolution of axial strain with differential stress for ST, CG, and ZG, respectively. Fig. 6b, Fig. 6d, and Fig. 6f illustrate the time-dependent evolution of axial strain and axial permeability for ST, CG, and ZG.

than the creep strain and steady-state creep rate of ST-2 under room temperature conditions (Figs. 5b and 6b). For CG, the axial strain during the creep phase for samples CG-4 and CG-5 reached 0.13 %, with steady-state creep rates of 1.87×10^{-9} and 2.07×10^{-9} higher than those of CG-2 (Figs. 5d and 6d). These results demonstrate increases in creep strain and the steady-state creep rates of ST and CG after heating, suggesting that elevated temperatures promote the creep behaviours of the sandstone, which may be due to the expansion of intra-and intergranular microcracks at high temperature, enhancing the creep deformation. In addition, the creep strain and steady-state creep rate of sample ST-5 is higher than those of ST-4 and ST-2, suggesting that pore pressure cycling has a significant impact on creep rates. Fluctuations in pore pressure may further disrupt the internal structure of the rock, accelerating the creep deformation of ST-5. In contrast, ZG-4 and ZG-5 both show axial strains of 0.10 %, with creep rates of $1.18.1 \times 10^{-9}$ and 1.25×10^{-9}, respectively, which are close to the creep strain and steady-state creep rate of ZG-2 at room temperature (Figs. 5f and 6f). This suggests that ZG exhibits higher stability, likely due to its denser internal structure, making it less susceptible to the effects of temperature and pore pressure fluctuations. In the third stage, with *Q* increasing to 49 MPa, axial strains of ST-4 and ST-5 during creep period further escalates to 0.31 % and 0.34 %, with steady-state creep rates of 4.76×10^{-9} and 5.40×10^{-9} (Fig. 6b). These results indicate that temperature and pore pressure cycling significantly accelerated creep of ST which can be attributed to greater microstructural changes under high pressure and high temperature conditions. These high temperatures and pressures induce microfracture propagation, further exacerbated by pore pressure changes. In comparison, the creep strain of CG-4 and CG-5 reach 0.23 %, with steady-state creep rates of 3.32×10^{-9} and 3.47×10^{-9} (Fig. 6d), both of which are higher than the creep strain and steady-state creep rate of CG-3 under ambient conditions (Figs. 5d and 6d). This indicates that temperature has an additional significant impact on the creep of CG under these high-pressure conditions. Although pore pressure cycling does influence the creep rate, its effect on the creep of CG is less pronounced compared to ST. The axial strains of ZG-4 and ZG-5 are relatively small, only 0.15 %, with low steady-state creep rates of 1.66×10^{-9} and 1.86×10^{-9}, respectively (Fig. 6f). These experimental results indicate that ZG exhibits relatively stable creep behaviour throughout the experimental process, with a small creep rate. Pore pressure cycling slightly accelerates its creep behaviour. This stability can be attributed to the low porosity and compact structure of ZG, its more compact internal structure, and fewer micro-fractures, which result in weaker responses to changes in external conditions (Zhang et al., 2020). These factors allow ZG to maintain good structural stability under high pressure and temperature conditions.

3.2. Permeability evolution

Fig. 5 illustrates the permeability evolution over time during the creep experiments for the three sandstones. Overall, the permeability of all three samples decreases with progressing creep. During loading, the permeability of ST-1, ST-2, and ST-3 decreases from 2.5×10^{-13} to 1.8×10^{-13} m^2, 1.4×10^{-13} m^2 and 9.4×10^{-14} m^2, corresponding to reductions of 31 %, 45 %, and 63 %, respectively. Upon entering the creep stage, the permeability decline rate gradually slows down. By the end of this stage, the permeability further reduces to 1.5×10^{-13} m^2, 1.2×10^{-13} m^2, and 8×10^{-14} m^2 for ST-1, ST-2, and ST-3, respectively. After unloading, the permeability of the samples partially recovers but remains below their initial levels, with overall losses of 14 %, 40 %, and 59 % (Fig. 5b). CG sandstone exhibits a different, lower permeability trend. After loading, the permeability of CG-1, CG-2, and CG-3 decreases from 3.9×10^{-13} m^2 to 3.5×10^{-13} m^2, 3.1×10^{-13} m^2, and 2.5×10^{-13} m^2, representing reductions of 10 %, 21 %, and 36 %, respectively. Following the creep stage, permeability further declines to 3.2×10^{-13} m^2, 2.7×10^{-13} m^2, and 2.1×10^{-13} m^2. After unloading, the permeability losses for these samples are 6 %, 20 %, and 25 % (Fig. 5d). This suggests that, compared to ST sandstone, CG sandstone with similar porosity shows higher permeabilities but lower permeability sensitivities. Furthermore, the low-porosity ZG sandstone exhibits even lower permeability. After loading, the permeability of ZG-1, ZG-2, and ZG-3 decreases from 8.9×10^{-15} m^2 to 7.4×10^{-15} m^2, 6.7×10^{-15} m^2, and 5.5×10^{-15} m^2, with reductions of 16.6 %, 24.4 %, and 37.8 %. At the end of the creep stage, it further drops to 6.7×10^{-15} m^2, 6.0×10^{-15} m^2, and 5.2×10^{-15} m^2. After unloading, these samples experience permeability losses of 13 %, 27 %, and 30 % (Fig. 5f).

Permeability tests were conducted on three sandstones during multistage creep experiments to investigate the effects of temperature and pore pressure cycling on their permeability evolution. The experimental results in Fig. 6 indicate that permeabilities of all sandstones generally exhibit a significant downward trend, particularly as the stress increases. Among them, the high-porosity ST sandstone exhibit a marked permanent loss in permeability after unloading, exceeding 60 %. Specifically, the permeability of ST-4 and ST-5 after unloading is 9.2×10^{-14} m^2, 8.2×10^{-14} m^2, respectively, showing losses of 64 % and 68 % compared to their initial, unstressed permeabilities (Fig. 6b). The permanent permeability losses of CG and ZG Sandstones is relatively small (<40 %) by the end of the experiments (Fig. 6d–f). Compared to room temperature conditions, elevated temperatures significantly reduce the permeability of the three sandstones, with the most pronounced effect observed for ST sandstone. This negative impact becomes more evident as both temperature and pressure increase. Specifically, ST-4 and ST-5 show slightly lower permeability in the first stage compared to ST-1 at room temperature (Figs. 5b and 6b). However, in the second and third stages, their permeability is significantly lower than that of ST-2 and ST-3, indicating that after high-temperature treatment, the permeability of ST-4 and ST-5 under the same stress conditions is markedly reduced compared to that of ST sandstone at room temperature. CG Sandstone exhibits a similar pattern, with permeability decreasing as temperature rises. In contrast, while elevated temperatures negatively affect the permeability of ZG, the impact is not as significant. Additionally, pore pressure cycling significantly enhances the permeability of ST Sandstone. Under identical temperature and pressure conditions, the permeability of ST-5 Sandstone is higher than that of ST-4, particularly during the high-temperature and stress stages (Fig. 6b). However, this trend is not as pronounced in CG and ZG.

4. Discussion

4.1. Deformation mechanisms of porous sandstones

4.1.1. Elastic mechanisms of porous sandstone

During the experiments, all three sandstones exhibited significant elastic deformation, as indicated by the nearly linear part of the stress-strain curves. Common microscopic mechanisms of elastic deformation in sandstones include elastic deformation at grain contact points, elastic compression of pores and microcracks, and elastic deformation of rigid cements between grains (Elata and Dvorkin, 1996; Mindlin, 1949; Zimmerman, 1990). As shown in Fig. 7, the high-porosity ST and CG sandstones, which primarily exhibit point and line contacts between grains due to weaker cementation, have lower Young's Moduli of 4.4 GPa and 6.8 GPa, respectively. Under external stress, the contact points between grains experience minor elastic deformation, primarily through compression and slight slip at the contact interfaces, resulting in reversible deformation of the overall structure. Upon the stress release, these contact points recover to their original state. Additionally, due to the high porosity of ST and CG, the pores do not experience significant fluid flow during the elastic deformation phase, and pore compression remains reversible. Therefore, the elastic deformation in ST and CG is predominantly governed by elastic deformation at grain contacts and the elastic compression of pores. Conversely, ZG is characterised by smaller grain contacts, low porosity, and contact modes between grains that are primarily line and surface contacts (Fig. 7e). In comparison to ST and CG, ZG exhibits larger contact areas between grains, allowing it to withstand greater stress and mitigate stress concentrations (Heap et al., 2009; Wong and Baud, 2012). These contact modes typically result in higher strength and stiffness, with a Young's Modulus of 12.9 GPa. Furthermore, despite the high degree of cementation, which is mainly through plastic clay minerals (Fig. 7f), the elastic deformation mechanism in ZG is mainly related to elastic deformation at particle contacts, elastic compression of pores, and microcracks.

4.1.2. Inelastic mechanisms of porous sandstone

The inelastic deformation of sandstone is usually the result of multiple micro-mechanisms acting in combination. Grain slip and grain rearrangement, grain breakage, and the breakdown of cements all contribute to the inelastic deformation of sandstone. These micro-mechanisms not only affect the long-term mechanical properties but also have significant impact on its transport properties (Baud et al., 2015, 2017; Pijnenburg et al., 2018, 2019; Pijnenburg and Spiers, 2020). Mechanical data reveal that all three sandstones exhibit cumulative, irrecoverable inelastic strain after unloading, especially samples subjected to high stress and high temperature conditions, which often accumulate more inelastic strain (Figs. 5 and 6). It is shown that high-porosity ST and CG exhibit more inelastic axial strain than low-porosity ZG under the same stress conditions. As shown in Fig. 7b and c, CG-3 develops a large number of intragranular and transgranular cracks which differs from the low-density intragranular cracks observed in CG-2 at lower temperature. Their formation and propagation are

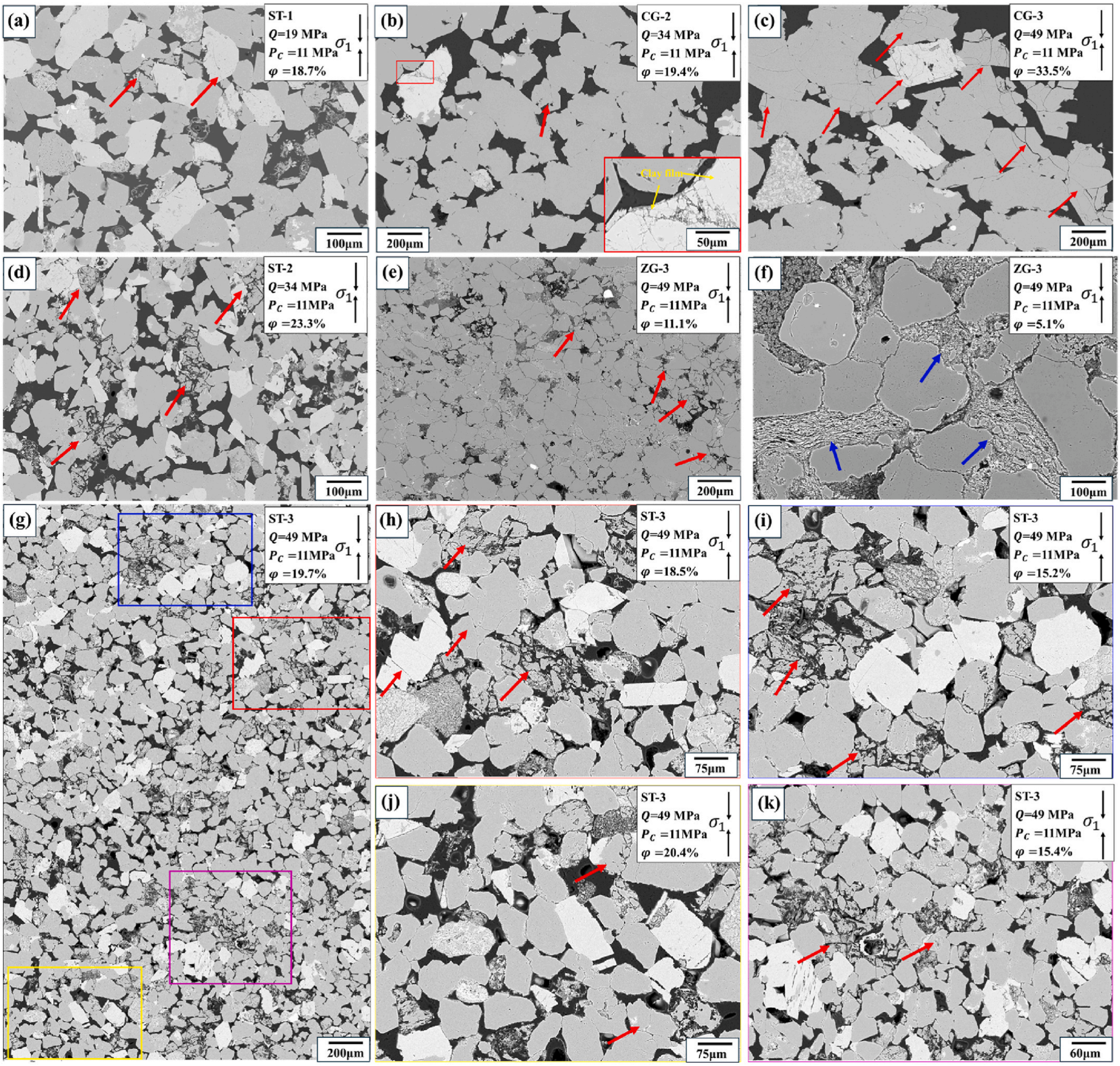

Fig. 7. SEM images of three sandstones after the experiments. Fig. 7a, Fig. 7d and Fig. 7g are SEM images of ST sandstone after creep experiments under different differential stress conditions. Fig. 7h–k are enlarged images of the regions within the red, blue, yellow, and purple boxes in montaged Fig. 7b and Fig. 7c are SEM images of CG sandstone after creep experiments under different differential stress conditions. Fig. 7e and Fig. 7f are SEM images of ZG sandstone after creep experiments under a differential stress of 49 MPa.

irreversible, manifesting as permanent inelastic strain at the macroscopic level. The development of these cracks is closely related to the contact modes within the sandstone. As differential stress increases, stress concentrations occur at the points of contact between grains, leading to the initiation and propagation of cracks (Wong et al., 1997; Zhang et al., 1990). Additionally, clay films are observed consolidating the quartz and calcite grains within CG-2 (Fig. 7b). Pijnenburg and Spiers (2020) show that the inelastic strain in weakly cemented porous sandstones can develop through compaction and the local slip on intergranular clay films under low-stress conditions. Notably, a significant number of fractured feldspar and quartz clusters are observed within the high-porosity ST sandstone in Fig. 7g–k. As stress increases, the development of these fractured clusters becomes more pronounced. The fragments from these clusters are dispersed throughout the sandstone pores, resulting in a more complex pore structure. These clusters are surrounded by intact quartz grains, likely due to their typically rounded morphology and higher mechanical strength. In contrast, feldspar and quartz clusters exhibit irregular shapes, making them more susceptible to break under stress, particularly due to stress concentration on point contacts and the cleavage planes in feldspar. These internally developed feldspar and quartz clusters manifest as distinct shear bands at the core scale, as indicated by the red lines in Fig. 8b and c. The development of these shear bands affects porosity, leading to compartmentalisation within the sandstone. Compared to the high-porosity ST and CG sandstones, the low-porosity ZG sandstone exhibits a lower density of intragranular cracks, with the compression of clay cements

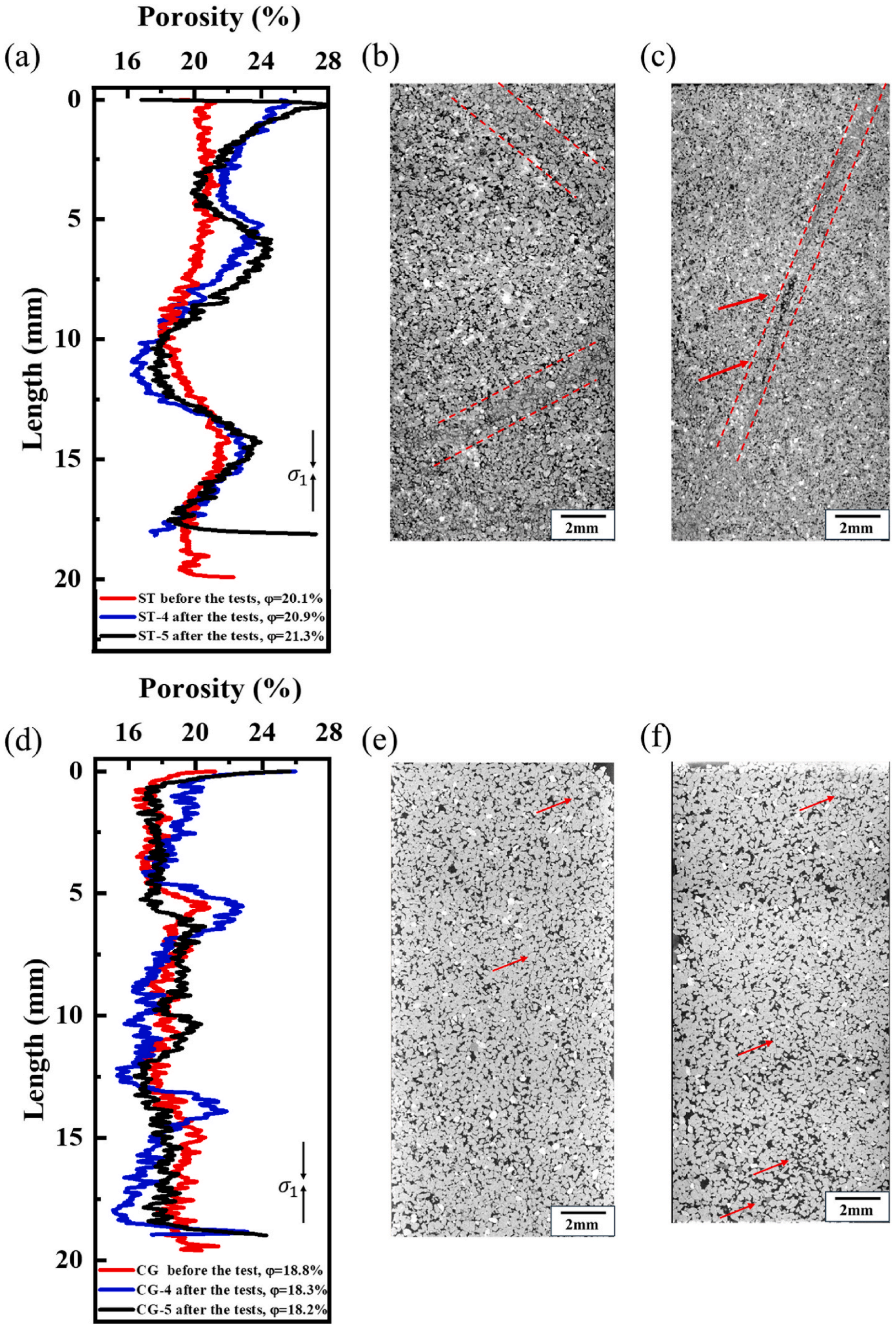

Fig. 8. Porosity variations and vertical CT images of three sandstones after multi-level stress creep experiments.

between grains potentially being one of significant micro-mechanism contributing to its inelastic deformation (Pijnenburg and Spiers, 2020).

4.2. Microstructural variations of sandstones and effects on transport properties

4.2.1. Porosity variations after the experiments

Microscopic observations indicate that the microstructures of the three sandstones undergo significant variations after the experiments. These variations include localised stress-induced compaction (evident from the tight grain contacts in Fig. 7a–f), and the consolidation of clay cements between grains (Fig. 7f), the formation of intra- and transgranular cracks (Fig. 7c), and the breakage and rearrangement of mineral grains (Fig. 7g–i). Consequently, these microstructural alterations affect porosity and permeability. To investigate the impact on porosity, three-dimensional porosity changes at the bulk plug scale were compared before and after the experiment (Fig. 8). For ST, the porosity curve before the experiments is relatively flat, with an average porosity of 20.1 % (Fig. 8a). In contrast, the porosity curves of ST-4 and ST-5 after the experiments show notable compartmentalisation, with three pronounced peaks observed at the 0–2.5 mm, 5–7.5 mm, and 12.5–15 mm sections. The overall porosity also increases to 20.9 % and 21.3 % respectively (Fig. 8a), suggesting that the microstructural changes in ST are dominated by dilatancy rather than compaction. CT images reveal the formation of shear bands composed of fragmented particles within ST-4 and ST-5 (Fig. 8b and Fig. 8c), which are likely the primary cause of

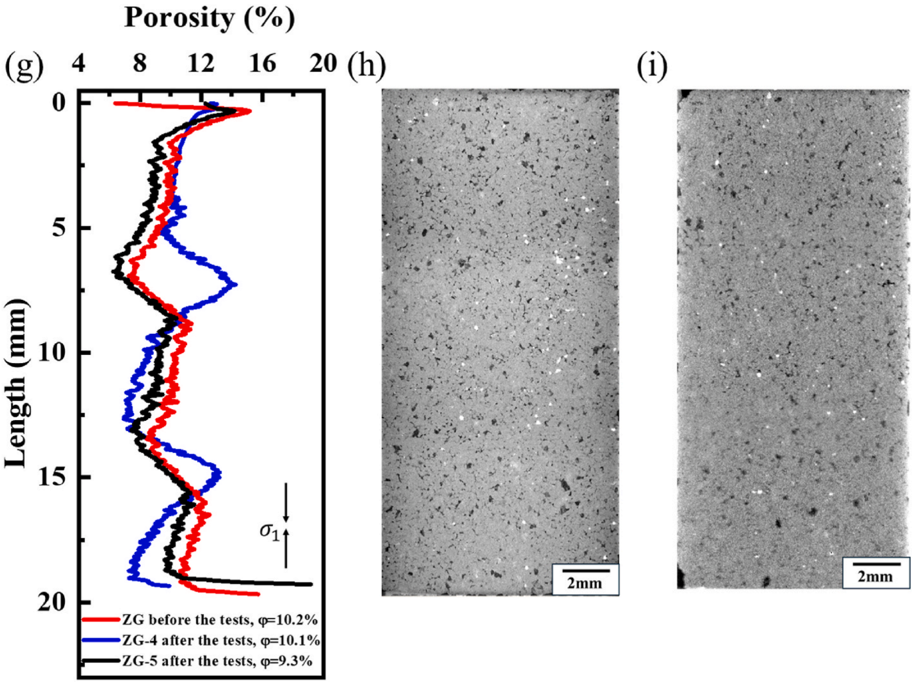

Fig. 8. (*continued*).

the increased porosity. SEM images indicate that these fragmented grains consist of feldspar and quartz clusters (Fig. 7g–i). Although the quartz surrounding these clusters exhibits stress-induced compaction (with grains closely packed, Fig. 7g–i), the fractured clusters create new voids, thereby increasing the overall porosity of the sandstone.

For CG, the porosity curve does not exhibit significant changes before and after the experiments. The peaks observed in certain sections of the porosity curve after the experiment may be related to the development of intra and transgranular cracks within the sandstone (Fig. 7c, Fig. 8e–f). Overall, the porosity of CG-4 and CG-5 are 18.2 % and 18.3 %, and therefore slightly lower than before the experiments, indicating that the microstructural changes are dominated by compaction. In contrast, for low-porosity ZG, the total porosity does not change significantly before and after the experiments, ranging between 9 and 10 %. The microstructural changes in this sandstone are also dominated by compaction, however the porosity curves of ZG-4 and ZG-5 show considerable morphological differences (Fig. 8g), which may be attributed to the presence of high clay contents between the sandstone grains, resulting in strong heterogeneity of the sandstone.

4.2.2. *Evolution of pore structure and effect on permeability*

Fig. 9 illustrates that during the creep experiments, permeability changes are closely related to axial strain. As axial strain increases, the permeability of all three sandstones gradually decreases. After unloading, although these sandstones experience a certain degree of elastic recovery due to the removal of external stress, the permeability cannot return to its initial level due to inelastic deformation accumulations. This permanent permeability loss is particularly evident after creep at high stress and temperature stages. This phenomenon can be explained by the microstructural changes that porous sandstones undergo during creep experiments (Bandara et al., 2021; Chu et al., 2021). Under low stress and temperature conditions, the grains within the sandstone may undergo slight displacements and rearrangements, leading to the compression of pores and micro-cracks which in turn results in a permeability decrease. As stress and temperature increase, local stress concentrations may develop at the contact points between grains, leading to the formation and propagation of intra- and transgranular cracks (Wong et al., 1997; Zhang et al., 1990). Furthermore, high temperature may induce inelastic deformations by mineral grain expansion and cracking, resulting in permanent changes to the pore structure (Fredrich and Wong, 1986; Wong and Brace, 1979). These changes cannot fully recover after unloading, exacerbating the permanent loss of permeability.

To quantitatively analyse the microscopic mechanisms of permanent permeability loss, pore network models (PNMs) were extracted at the whole-core scale before and after the experiments for all sandstone types, providing information on pore and throat size distributions, as well as topological properties such as coordination number and tortuosity (Fig. 10 and Table 3). As shown in Fig. 10a and Fig. 10b, most pores and throats in ST before the experiment are within the ranges of 40–160 μm and 30–80 μm. After multi-level stress creep experiments, the average pore and throat diameters in ST-4 and ST-5 decrease significantly, while the number of pores increases. Additionally, their coordination number decreases, and the tortuosity of pores increases. Microstructural observations and porosity evolution indicate that the increased porosity in ST-4 and ST-5 after the experiments is attributed to the extensive development of fractured feldspar and quartz clusters (Fig. 7g–k), which exist in the form of shear bands within the sandstone. These fractured clusters create new voids, increasing the overall porosity of the sandstone (Fig. 8a–c). However, the fine debris generated from cluster breakage fill and obstruct the throats, reducing both their number and average diameter. This process complicates the pore structure of the sandstone, significantly diminishing its connectivity and resulting in significant permeability loss (Fredrich et al., 1995; Ngwenya et al., 2003; Vajdova et al., 2004). For CG sandstone, the pore and throat sizes range from 40 to 200 μm and 20–80 μm, respectively, but its average pore and throat diameters, as well as its coordination number, are significantly larger than those of ST sandstone (Fig. 10c and d, Table 3). Compared to pre-experimental conditions, CG-4 and CG-5 show reduced average pore and throat diameters, along with a reduction in the number of pores and throats, and a general decrease in coordination number. Although SEM and CT images reveal extensive intra- and transgranular cracks within this sandstone (Fig. 7e), the total porosity of CG-4 and CG-5 decreases (Fig. 8d), suggesting that deformation is still dominated by compaction and consequently permeability reduction. While compaction narrows the pores and throats, it does not significantly alter

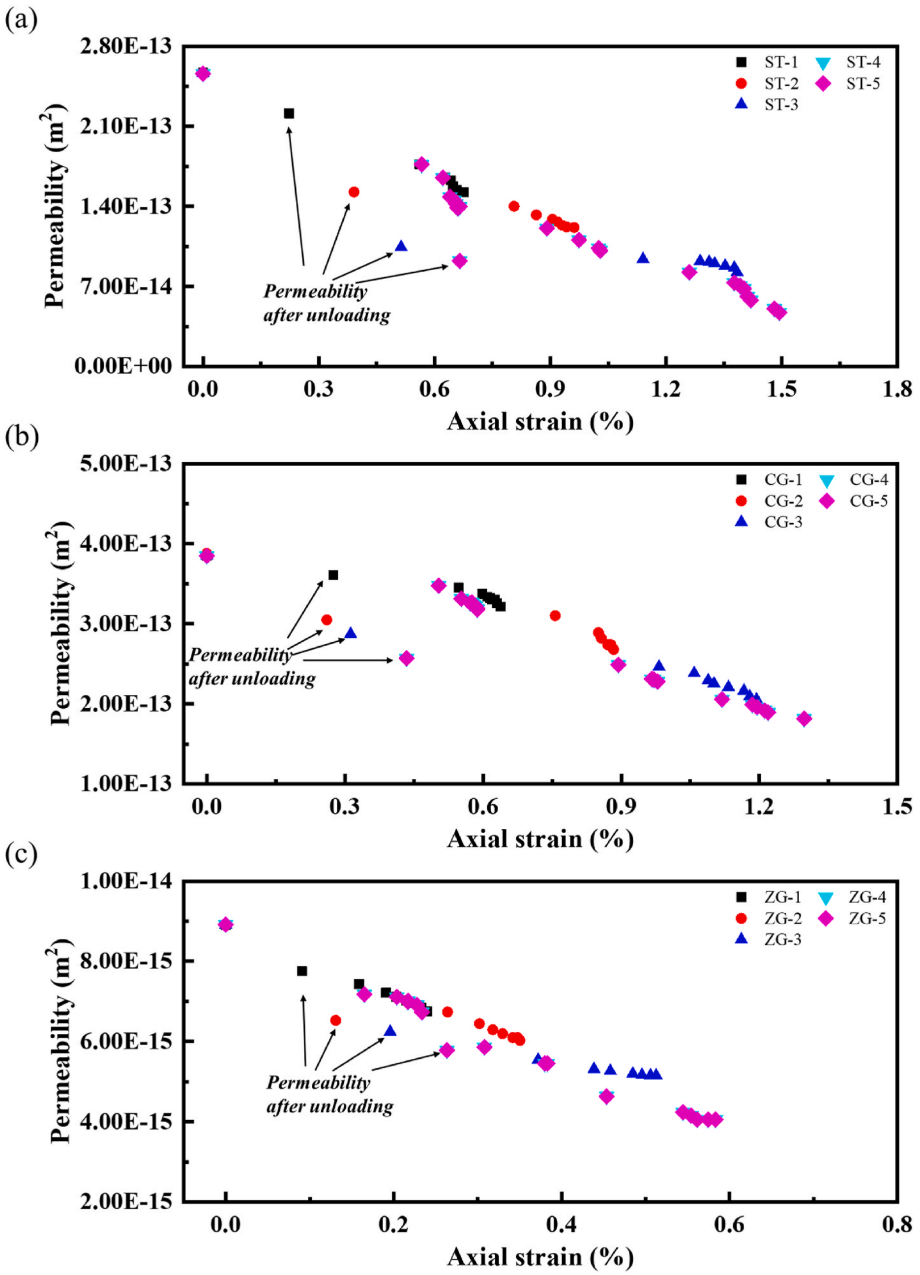

Fig. 9. Relationship between permeability and axial strain. The permeability reduction is closely related to axial strain. Notably, the significant decrease in permeability of ST sandstone is strongly associated with the development of internal shear bands. (a) ST; (b) CG; (c) ZG.

the pore tortuosity, resulting in less permeability loss for CG compared to ST sandstone (Table 3). In contrast to the two high-porosity sandstones, ZG has lower porosity, smaller pore and throat sizes, less developed connectivity, and higher pore tortuosity (Fig. 10e and Fig. 10f, Table 3), which are the main factors contributing to its lower permeability. Comparing pre- and post-experiment samples, the reduction in pore and throat numbers in ZG is likely related to compaction. Similar to CG, the deformation mechanism is dominated by compaction and therefore leads to the closure of pores and micro-cracks between grains, causing permeability loss (Dong et al., 2010; Wang et al., 2017).

4.2.3. *The effect of pore pressure cycling*

To investigate the effects of pore pressure cycling, creep tests were performed under identical axial stress, confining pressure, and temperature conditions to compare sandstones' responses to constant versus cyclically imposed pore pressure. The results indicate that cyclic pore pressure leads to an acceleration of creep, ultimately accumulating more inelastic strain. This is most pronounced in ST, followed by CG Sandstone and ZG sandstones. This can be attributed to the microstructure of ST, which is characterised by higher porosity, smaller grain size, and a significant amount of low-strength feldspar-quartz clusters with angular shapes (He et al., 2019; Heidaryan et al., 2023). Cyclic pore pressure variations induce localised stress concentrations within the sandstone, promoting the formation of microcracks that gradually develop into macroscopic fractures with repeated pressure changes (Tullis, 1983; Tullis and Yund, 1992)(Fig. 8c). These fractures not only increase the inelastic deformation of the rock but also alter its overall mechanical properties, which has been reported in previous studies (Asahina et al., 2019; Cerasi et al., 2018; Han et al., 2018; Noël et al., 2019). It should be noted that thermal effects were not considered a dominant factor in fracture development, as the maximum temperature applied was below 100 °C. At this temperature range, thermal stresses are generally

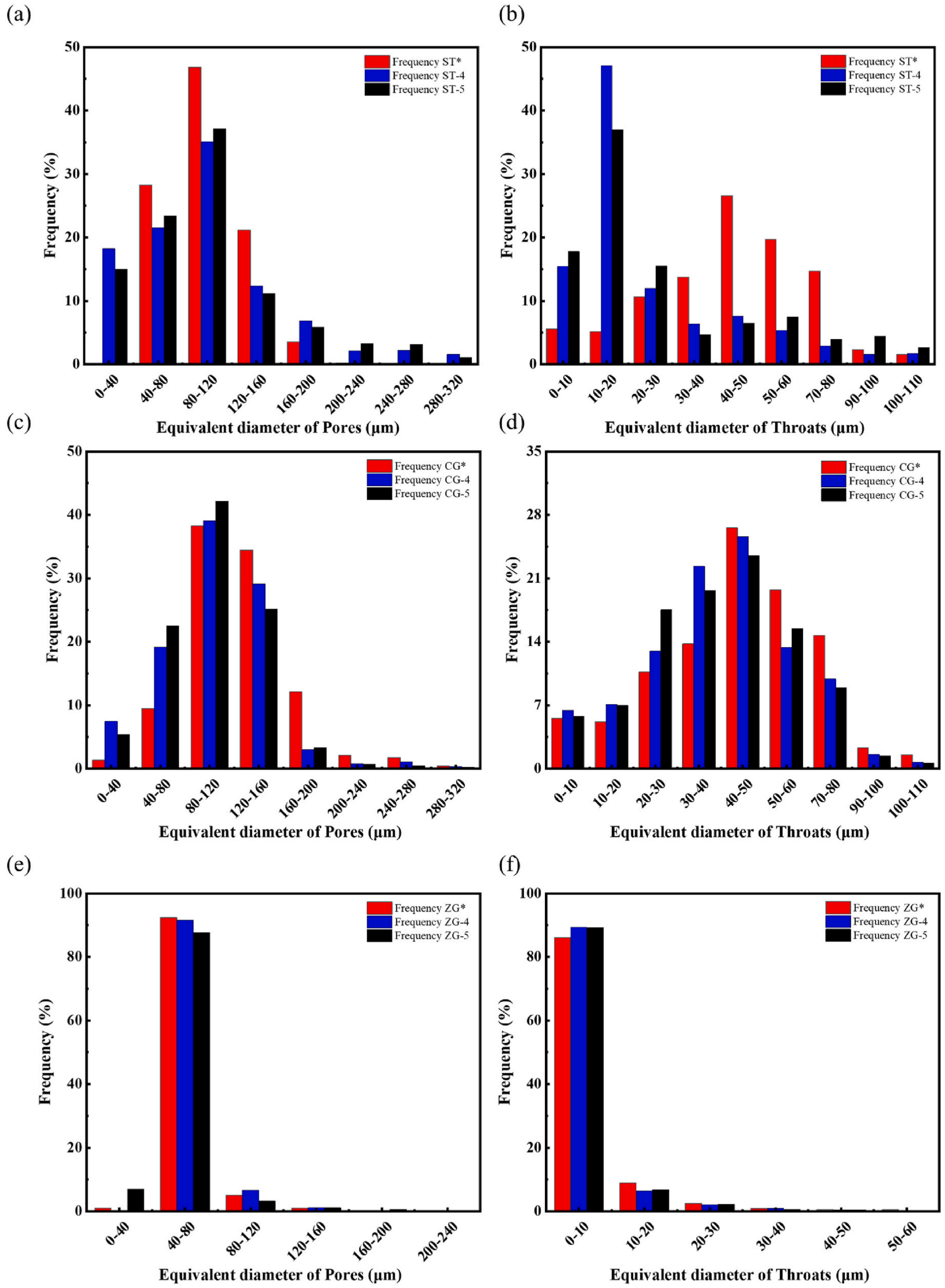

Fig. 10. Pore body and pore throat evolution before and after experiments. (a), (c), (e) show the pore size distributions and (b), (d), (f) the throat distributions of ST, CG, and ZG sandstones, respectively.

insufficient to induce significant microcracking in sandstones, and the observed macroscopic fractures in ST-5 are therefore primarily attributed to mechanical damage under cyclic loading. The fractures in ST are predominantly composed of fragmented feldspar-quartz clusters, which degrade the pore structure and result in a further reduction in permeability. Conversely, although CG also has a high porosity, its lower feldspar and higher quartz contents result in higher strength compared to ST sandstone. After pore pressure cycling, it does not exhibit

Table 3
Pore structure characteristics of three sandstones.

Rock type	NO.[a]	Pores	Total pore volume (μm^3)	Mean pore diameter (μm)	Mean Coordination Number	Number of pore throats	Mean throat diameter (μm)	Tortuosity
ST Sandstone	ST*	3.75×10^4	2.67×10^{11}	114.67	7.46	1.45×10^5	25.16	1.65
	ST-4	4.44×10^4	2.94×10^{11}	104.60	6.36	1.22×10^5	16.86	1.74
	ST-5	5.15×10^4	3.09×10^{11}	112.72	7.18	1.27×10^5	16.44	1.78
CG Sandstone	CG*	2.79×10^4	2.37×10^{11}	124.78	10.66	1.27×10^5	42.74	1.63
	CG-4	2.69×10^4	2.28×10^{11}	106.52	8.26	1.19×10^5	37.64	1.64
	CG-5	2.64×10^4	2.19×10^{11}	102.37	8.93	1.09×10^5	38.92	1.63
ZG Sandstone	ZG*	5.55×10^4	1.61×10^{11}	58.03	4.48	1.46×10^5	5.37	1.72
	ZG-4	4.96×10^4	1.39×10^{11}	58.27	4.48	1.36×10^5	4.86	1.72
	ZG-5	4.88×10^4	1.52×10^{11}	57.59	4.27	1.30×10^5	5.02	1.72

Note: *a*. Pore structure data for ST*, CG* before the experiments obtained from micro-CT scans of twin plugs, while initial pore structure data for ZG* obtained from ZG-5.

significant macroscopic cracking. Instead, repeated pressure changes cause greater pore compression (Table 3), leading to higher axial strains. In contrast, ZG sandstone, with its lower porosity and smaller pores, is less affected by changes in pore pressure, resulting in minimal structural deformation under cyclic pore pressure, thereby exhibiting greater stability. Additionally, the larger grain sizes of ZG and predominantly line and surface contacts between grains effectively mitigate localised stress concentrations, providing it with higher strength. This high strength enables ZG to better resist deformation caused by external pressures and pore pressure fluctuations.

4.3. *Creep models for porous sandstones under in situ conditions*

Underground hydrogen storage involves the long-term retention of hydrogen within porous sandstone formations, where the creep behaviour of the reservoir rocks directly influences the safety and stability of the storage system. Therefore, accurate prediction of the creep behaviour is essential for the development of effective hydrogen storage strategies and the design of safe and reliable storage facilities. To achieve this, it is necessary to establish models capable of describing the creep behaviour of porous sandstones under *in situ* conditions. Creep models are generally classified into two main categories: those based on empirical fitting and those grounded in rheological physical models (Brantut et al., 2012; Paraskevopoulou et al., 2017; Zheng et al., 2015). Rheological models simulate the creep behaviour of rocks by utilising mechanical analogues such as elastic springs, viscous dashpots, plastic sliders, and brittle yielding elements, arranged in series or parallel configuration (Fossen, 2016). Fig. 11 illustrates the typical creep characteristics of rocks. Under constant loading conditions, rock creep typically progresses through three stages: primary creep, secondary creep, and tertiary creep. During the primary creep stage, the strain rate gradually decreases, primarily due to stress redistribution and adjustments within the internal microstructure. This stage is often referred to as transient creep. As the strain rate stabilizes, the rock deformation enters the secondary creep stage, also known as the steady-state creep phase. Ultimately, when the strain rate begins to accelerate, the rock transitions into the tertiary creep stage, which may culminate in brittle failure (Brantut et al., 2013; Paraskevopoulou et al., 2017).

Previous research indicates that commonly used rheological models can effectively reproduce primary and secondary creep but often fail to accurately simulate tertiary creep (Liu et al., 2019; Paraskevopoulou et al., 2017; Wu et al., 2020). The primary creep is typically characterised by viscoelastic deformation that delays the adjustment to a new equilibrium state and may involve some irreversible behaviour, leading to a decrease in strain accumulation over time. The Kelvin model is frequently employed to simulate this stage (Pajic-Lijakovic, 2021; Serra-Aguila et al., 2019). The secondary creep is marked by a stable strain rate over time, accompanied by inelastic deformation. The Maxwell viscoelastic model is commonly used to phenomenologically describe this stage. However, the tertiary creep is characterised by a sudden increase in strain rate due to stress-driven weakening or crack interaction, ultimately leading to rock failure (Ranalli, 1995). Traditional rheological models do not account for the physical mechanisms associated with microcrack initiation and propagation, making it challenging to accurately simulate tertiary creep (Paraskevopoulou et al., 2017). In this study, it can be observed that under *in situ* conditions, the stresses experienced by all sandstones were significantly lower than their strength limits, and their strain-time curves did not exhibit distinct tertiary creep characteristics. The strain rate gradually decreased and stabilised over time. Therefore, it is reasonable to utilise the Burgers model, which combines the Maxwell model and the Kelvin-Voigt model (Chen et al., 2023; Cong and Hu, 2017; Serra-Aguila et al., 2019), to simulate the creep behaviour of the three types of sandstone under *in situ* conditions.

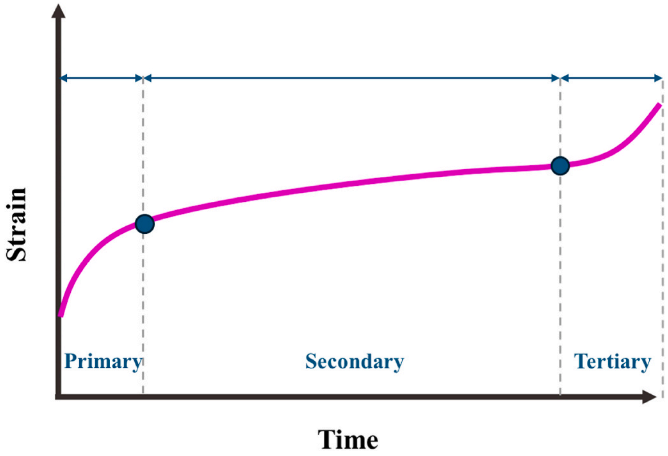

Fig. 11. Schematic diagram of typical rock creep behaviour. Rock creep typically progresses through three stages: primary, secondary and tertiary creep.

The Burgers creep model is composed of a series combination of the Maxwell model and the Kelvin-Voigt model (Fig. 12). The Maxwell model consists of a spring and a dashpot arranged in series, while the Kelvin-Voigt model is composed of a spring and a dashpot arranged in parallel. In this model, the spring element represents the instantaneous elastic response, and the dashpot element represents the time-dependent viscous characteristics (Fossen, 2016). Within the Burgers creep model, the Kelvin-Voigt model is used to describe the transient (i.e., primary creep) phase, while the Maxwell model primarily accounts for the instantaneous strain and the secondary creep. In conventional triaxial compression tests, the applied stress conditions are typically $\sigma_1 > \sigma_2 = \sigma_3$. Additionally, confining pressure is usually applied before deformation measurements are taken. Consequently, the volumetric strain

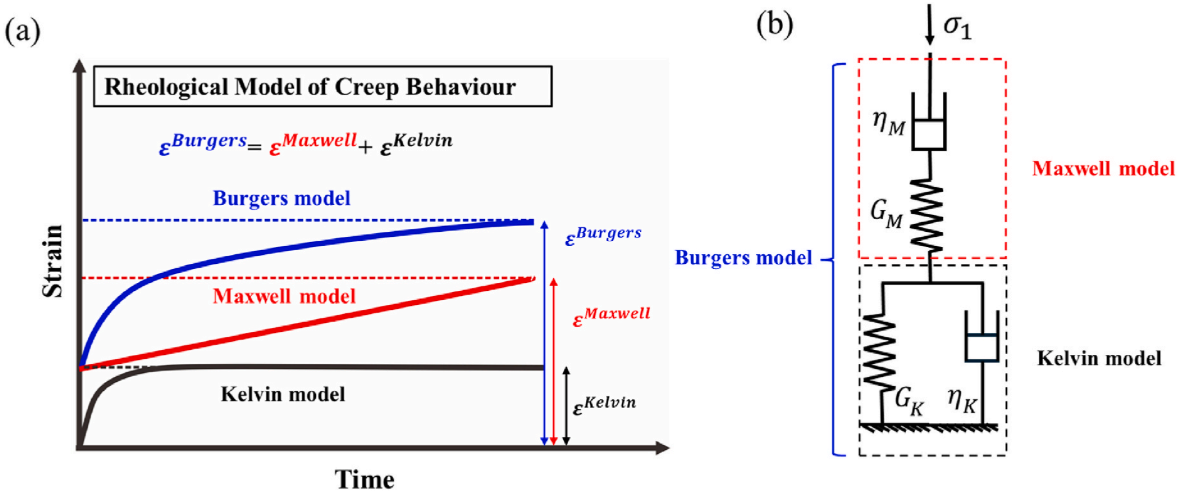

Fig. 12. Rheological models of creep behaviour. (a) The strain vs strain curve of rheological models; (b) Equivalent components of rheological models.

caused by confining pressure is not considered in the three-dimensional strain equation of the Burgers creep model. The axial strain of the Maxwell model under conventional triaxial compression test conditions is given by (Wang and Li, 2018):

$$\varepsilon^{Maxwell} = \frac{(\sigma_1 - \sigma_3)}{9K} + \frac{(\sigma_1 - \sigma_3)}{3G_M} + \frac{(\sigma_1 - \sigma_3)t}{3\eta_M} \tag{4}$$

where K, G_M and η_M are the bulk modulus, shear modulus, and viscosity coefficient of the Maxwell model, respectively. The axial viscoelastic strain of the Kelvin-Voigt model caused by deviatoric stress is represented as:

$$\varepsilon^{Kelvin} = \frac{(\sigma_1 - \sigma_3)}{3G_K}\left(1 - exp\left(-\frac{(G_K t)}{\eta_K}\right)\right) \tag{5}$$

where G_K and η_K are the shear modulus and viscosity coefficient of the Kelvin-Voigt model, respectively. By combining equations (4) and (5), the axial strain of the Burgers creep model under a three-dimensional stress state can be obtained (Zhao et al., 2017):

$$\varepsilon^{Burgers} = \frac{(\sigma_1 - \sigma_3)}{9K} + \frac{(\sigma_1 - \sigma_3)}{3G_M} + \frac{(\sigma_1 - \sigma_3)t}{3\eta_M} + \frac{(\sigma_1 - \sigma_3)}{3G_K}\left(1 - exp\left(-\frac{(G_K t)}{\eta_K}\right)\right) \tag{6}$$

The bulk modulus K of three sandstone is calculated from Young's modulus and Poisson's ratio according to (Fjaer et al., 2008):

$$K = \frac{E}{3(1 - 2v)} \tag{7}$$

Based on the results of the creep tests, this study employs the Levenberg-Marquardt algorithm combined with the least squares method to fit the parameters (Liu et al., 2017; Wei et al., 2022), thereby obtaining the viscoelastic parameters G_M, G_K, η_M, η_K of the Burgers model, as shown in Table 4. The results indicate that the model accurately describes the experimental data, as shown in Fig. 13 and Table 4.

Table 4
Parameters of the creep models for the three types of sandstone under *in situ* conditions.

Sandstone type	Q (MPa)	T (°C)	G_M (GPa)	η_M (GPa h)	G_K (GPa)	η_K (GPa h)	R^2
ST	19	49	1.52	935	5.50	0.722	0.98
	34	69	1.71	2113	5.87	17.71	0.99
	49	88	1.68	1688	8.66	49.83	0.98
CG	19	49	1.59	1430	5.96	3.00	0.98
	34	69	1.48	1957	15.14	66.05	0.95
	49	88	1.72	1757	16.86	99.77	0.97
ZG	19	49	4.89	1419	13.06	1.34	0.98
	34	69	4.89	6483	11.36	80.38	0.97
	49	88	4.34	7261	13.12	78.62	0.99

4.4. Implications for underground hydrogen storage

During UHS operations, the mechanical responses of reservoir rocks and changes in their permeability directly affect the stability of the reservoir and the efficiency of hydrogen storage. By conducting creep experiments on three different types of sandstone under *in situ* conditions for UHS at the laboratory scale, it can be revealed the deformation mechanisms and their impact on transport properties. In creep experiments, the porous and feldspar-rich ST sandstone exhibits unstable mechanical properties. Numerous feldspar and quartz clusters within the rock contribute to its vulnerability. As temperature and stress increases (corresponding to greater reservoir depth), these weak clusters tend to fracture due to stress concentrations, resulting in extensive cracks. They not only affect reservoir stability but also lead to a substantial decline in permeability, as the fragmented debris block pore channels, further deteriorating reservoir performance. Additionally, under cyclic pore pressure conditions, microcracks within this sandstone may propagate and even form macroscopic fractures, potentially triggering fault activation and undermining the stability of the hydrogen storage reservoir. Thus, special attention should be given to the burial depth and stress concentration regions of such reservoirs in UHS applications. In contrast, the homogeneous, high-porosity CG sandstone demonstrates good stability during the experiments. Unlike ST sandstone, the deformation of CG is dominated by compaction. With ongoing compression, the porosity gradually decreases, leading to a reduction in permeability, which eventually stabilizes. This suggests that quartz-rich, high-porosity sandstones like CG may exhibit greater stability during UHS operations, making them suitable for long-term UHS operations. Nevertheless, with increasing burial depth, the potential for grain breakage should be considered as it may impact the overall stability of these reservoirs. In comparison, the low-porosity ZG sandstone is characterised by large and tightly packed grains, exhibiting excellent mechanical properties. However, its inherently low porosity and permeability may restrict hydrogen flow, requiring careful consideration of injection pressure and reservoir depth in the design of UHS systems to optimize storage efficiency.

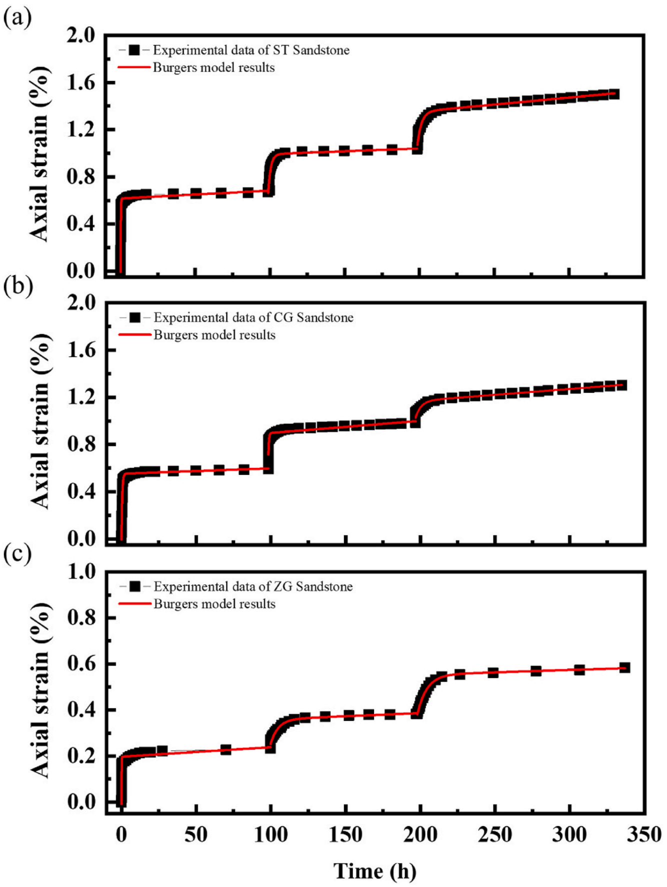

Fig. 13. Comparison of Burgers model results and experimental results during multi-level stress creep tests under *in situ* conditions for three sandstones.

5. Conclusion

In this study, creep experiments were conducted on three porous sandstones under simulated *in situ* conditions representative of underground hydrogen storage (UHS) operations at the laboratory scale, to investigate their mechanical responses and permeability evolution. The main findings are as follows.

1.During the experiments, all three sandstones exhibit stable creep behaviour, with the steady-state creep rate increasing as temperature and stress increases. The high-porosity ST and CG sandstones show higher steady-state creep rates under the same conditions compared to the low-porosity ZG sandstone, highlighting the strong influence of porosity on creep susceptibility.

2.The evolution of permeability is strongly coupled with axial strain accumulation. A permanent loss of permeability is observed in all sandstones after unloading, indicating irreversible damage to the pore structure. This irreversible permeability reduction becomes more pronounced with increasing creep strain and elevated temperature, revealing a direct link between time-dependent deformation and transport property degradation.

3.Microstructural analysis reveals that the deformation mechanism of the high-porosity ST sandstone is dominated by dilatancy. Although shear-induced deformation causes the feldspar and quartz clusters to fracture, creating new voids and increasing the overall porosity, the fractured debris from these clusters block the throats, complicating the pore structure and leading to a significant permeability loss. The deformation mechanisms of CG and ZG sandstones, on the other hand, are dominated by compaction, with pore compression and microcrack closure being the primary causes of permeability losses.

4.Pore pressure cycling increases the creep rate of the sandstones, accumulating more inelastic strain. This trend is most evident in the ST, followed by CG sandstone, with ZG sandstone being the least affected. This can be attributed to a significant amount of angular, low-strength feldspar-quartz clusters within the ST Sandstone. Pore pressure cycling causes localised stress concentrations within the sandstone, promoting the formation of microcracks. These gradually develop into macroscopic fractures with repeated pressure changes. In contrast, CG and ZG are less affected by pore pressure changes and demonstrated better stability.

5.The Burgers model is used to fit the creep data of the three sandstones under *in situ* conditions, and a good match is achieved, indicating that this model can effectively describe the creep behaviour of the sandstones tested ion this study. Its successful application confirms its suitability for describing time-dependent deformation in porous reservoir rocks and provides a predictive framework for assessing long-term mechanical stability in underground hydrogen storage operations.

CRediT authorship contribution statement

Ming Wen: Writing – review & editing, Writing – original draft, Visualization, Methodology, Investigation, Formal analysis, Data curation, Conceptualization. **Qianyou Wang:** Writing – original draft, Visualization, Methodology, Formal analysis, Conceptualization. **Nick Harpers:** Writing – review & editing, Writing – original draft, Methodology, Formal analysis, Conceptualization. **Nathaniel Forbes Inskip:** Writing – review & editing, Writing – original draft, Methodology, Formal analysis, Conceptualization. **Jim Buckman:** Writing – review & editing, Visualization, Supervision, Methodology, Data curation, Conceptualization. **Kamaljit Singh:** Writing – review & editing, Writing – original draft, Visualization, Supervision, Methodology, Conceptualization. **Paul Miller:** Software, Methodology. **Andreas Busch:** Writing – review & editing, Writing – original draft, Supervision, Methodology, Conceptualization.

Declaration of competing interest

The authors declare that they have no known competing financial interests or personal relationships that could have appeared to influence the work reported in this manuscript. Furthermore, the authors affirm that this research was conducted independently and without any external influence from funding bodies, institutions, or other entities that might benefit from the results.

All data presented in this study were produced and analysed with academic integrity, and no commercial or personal bias was introduced. The authors have ensured full transparency in methodology, analysis, and conclusions.

Acknowledgements

We would like to express our gratitude to the James Watt Scholarship from EGIS at Heriot-Watt University for its funding support, and to Jack Irvine for his great help in making the Harper's THMC Flow Workbench operational. Also, we sincerely thank the reviewers and editors for their valuable comments and constructive suggestions, which have significantly improved the quality of this paper.

Data availability

Data will be made available on request.

References

Asahina, D., Pan, P.-Z., Sato, M., Takeda, M., Takahashi, M., 2019. Hydraulic and mechanical responses of porous sandstone during pore pressure-induced reactivation of fracture planes: an experimental study. Rock Mech. Rock Eng. 52 (6), 1645–1656.

Bandara, K.M.A.S., et al., 2021. An experimental investigation of the effect of long-term, time-dependent proppant embedment on fracture permeability and fracture aperture reduction. Int. J. Rock Mech. Min. Sci. 144.

Baud, P., Exner, U., Lommatzsch, M., Reuschlé, T., Wong, T.f., 2017. Mechanical behavior, failure mode, and transport properties in a porous carbonate. J. Geophys. Res. Solid Earth 122 (9), 7363–7387.

Baud, P., Reuschlé, T., Ji, Y., Cheung, C.S.N., Wong, T.f., 2015. Mechanical compaction and strain localization in Bleurswiller sandstone. J. Geophys. Res. Solid Earth 120 (9), 6501–6522.

Brantut, N., Baud, P., Heap, M.J., Meredith, P.G., 2012. Micromechanics of brittle creep in rocks. J. Geophys. Res. Solid Earth 117 (B8).

Brantut, N., Heap, M.J., Meredith, P.G., Baud, P., 2013. Time-dependent cracking and brittle creep in crustal rocks: a review. J. Struct. Geol. 52, 17–43.

Brice, J.C., Levin, H.L., 1962. Porosity and permeability experiments for general geology laboratory. J. Geol. Educ. 10 (3), 81–90.

Brzesowsky, R.H., Hangx, S.J.T., Brantut, N., Spiers, C.J., 2014. Compaction creep of sands due to time-dependent grain failure: effects of chemical environment, applied stress, and grain size. J. Geophys. Res. Solid Earth 119 (10), 7521–7541.

Cerasi, P., et al., 2018. Experimental investigation of injection pressure effects on fault reactivation for CO2 storage. Int. J. Greenh. Gas Control 78, 218–227.

Chen, D., Wang, L., Versaillot, P.D., Sun, C., 2023. Triaxial creep damage characteristics of sandstone under high crustal stress and its constitutive model for engineering application. Deep Underground Sci. Eng. 2 (3), 262–273.

Chu, Z., et al., 2021. Evaluating the microstructure evolution behaviors of saturated sandstone using NMR testing under uniaxial short-term and creep compression. Rock Mech. Rock Eng. 54 (9), 4905–4927.

Chu, Z., et al., 2022. Micro-mechanism of brittle creep in saturated sandstone and its mechanical behavior after creep damage. Int. J. Rock Mech. Min. Sci. 149.

Cong, L., Hu, X., 2017. Triaxial rheological property of sandstone under low confining pressure. Eng. Geol. 231, 45–55.

Darcy, H., 1856. Les fontaines publiques de la ville de Dijon: exposition et application des principes à suivre et des formules à employer dans les questions de distribution d'eau, vol. 1. Victor dalmont.

Dong, H., Blunt, M.J., 2009. Pore-network extraction from micro-computerized-tomography images. Phys. Rev.E 80 (3), 036307.

Dong, J.-J., et al., 2010. Stress-dependence of the permeability and porosity of sandstone and shale from TCDP Hole-A. Int. J. Rock Mech. Min. Sci. 47 (7), 1141–1157.

Elata, D., Dvorkin, J., 1996. Pressure sensitivity of cemented granular materials. Mech. Mater. 23 (2), 147–154.

Fjaer, E., Holt, R.M., Horsrud, P., Raaen, A.M., 2008. Petroleum Related Rock Mechanics. Elsevier.

Fossen, H., 2016. Structural Geology. Cambridge university press.

Fredrich, J., Menéndez, B., Wong, T.-F., 1995. Imaging the pore structure of geomaterials. Science 268 (5208), 276–279.

Fredrich, J.T., Wong, T.f., 1986. Micromechanics of thermally induced cracking in three crustal rocks. J. Geophys. Res. Solid Earth 91 (B12), 12743–12764.

Han, B., Shen, W.Q., Xie, S.Y., Shao, J.F., 2018. Influence of pore pressure on plastic deformation and strength of limestone under compressive stress. Acta Geotechnica 14 (2), 535–545.

Hangx, S.J.T., Spiers, C.J., Peach, C.J., 2010. Creep of simulated reservoir sands and coupled chemical-mechanical effects of CO2 injection. J. Geophys. Res. Solid Earth 115 (B9).

Harpers, N., Wen, M., Miller, P., Hangx, S., Busch, A., 2023. The Harpers THMC flow bench: a triaxial multi-reactor setup for the investigation of long-term coupled thermo-hydro-mechanical-chemical fluid-rock interaction. Rev. Sci. Instrum. 94 (9).

Hawkins, A., McConnell, B., 1991. Sandstones as geomaterials. Q. J. Eng. Geol. Hydrogeol. 24 (1), 135–142.

He, W., Chen, K., Hayatdavoudi, A., Sawant, K., Lomas, M., 2019. Effects of clay content, cement and mineral composition characteristics on sandstone rock strength and deformability behaviors. J. Petrol. Sci. Eng. 176, 962–969.

Heap, M.J., Baud, P., Meredith, P.G., 2009. Influence of temperature on brittle creep in sandstones. Geophys. Res. Lett. 36 (19).

Heidaryan, P., Asef, M., Khademi Hamidi, J., Talkhablou, M., 2023. The relationship between mechanical properties and quartz-feldspar composition of sedimentary rocks. J. Anal. Numer. Method. Mining Eng. 13 (36), 1–13.

Heinemann, N., et al., 2021. Enabling large-scale hydrogen storage in porous media–the scientific challenges. Energy Environ. Sci. 14 (2), 853–864.

Iglauer, S., 2022. Optimum geological storage depths for structural H2 geo-storage. J. Petrol. Sci. Eng. 212, 109498.

Kibikas, W.M., Bauer, S.J., 2021. Mechanical response of castlegate sandstone under hydrostatic cyclic loading. Geofluids 2021, 1–18.

Kumar, K.R., Honorio, H., Chandra, D., Lesueur, M., Hajibeygi, H., 2023. Comprehensive review of geomechanics of underground hydrogen storage in depleted reservoirs and salt caverns. J. Energy Storage 73, 108912.

Lankof, L., Tarkowski, R., 2020. Assessment of the potential for underground hydrogen storage in bedded salt formation. Int. J. Hydrogen Energy 45 (38), 19479–19492.

Liu, H.Z., Xie, H.Q., He, J.D., Xiao, M., Zhuo, L., 2017. Nonlinear creep damage constitutive model for soft rocks. Mech. Time-Dependent Mater. 21, 73–96.

Liu, L., Xu, W.Y., Wang, H.L., Wang, W., Wang, R.B., 2016. Permeability evolution of granite gneiss during triaxial creep tests. Rock Mech. Rock Eng. 49 (9), 3455–3462.

Liu, Y., Wang, W., He, Z., Lyv, S., Yang, Q., 2019. Nonlinear creep damage model considering effect of pore pressure and analysis of long-term stability of rock structure. Int. J. Damage Mech. 29 (1), 144–165.

McPherson, M., Johnson, N., Strubegger, M., 2018. The role of electricity storage and hydrogen technologies in enabling global low-carbon energy transitions. Appl. Energy 216, 649–661.

Miall, A.D., Arush, M., 2001. The Castlegate Sandstone of the Book Cliffs, Utah: sequence stratigraphy, paleogeography, and tectonic controls. J. Sediment. Res. 71 (4), 537–548.

Mindlin, R.D., 1949. Compliance of elastic bodies in contact.

Mortazavi, A., Atapour, H., 2018. An experimental study of stress changes induced by reservoir depletion under true triaxial stress loading conditions. J. Petrol. Sci. Eng. 171, 1366–1377.

Muhammed, N.S., et al., 2022. A review on underground hydrogen storage: insight into geological sites, influencing factors and future outlook. Energy Rep. 8, 461–499.

Ngwenya, B.T., Kwon, O., Elphick, S.C., Main, I.G., 2003. Permeability evolution during progressive development of deformation bands in porous sandstones. J. Geophys. Res. Solid Earth 108 (B7).

Noël, C., Passelègue, F.X., Violay, M., 2021. Brittle faulting of ductile rock induced by pore fluid pressure build-up. J. Geophys. Res. Solid Earth 126 (3).

Noël, C., Pimienta, L., Violay, M., 2019. Time-dependent deformations of sandstone during pore fluid pressure oscillations: implications for natural and induced seismicity. J. Geophys. Res. Solid Earth 124 (1), 801–821.

Pajic-Lijakovic, I., 2021. The Basic Concept of Viscoelasticity, Viscoelasticity and Collective Cell Migration. Elsevier, pp. 21–46.

Paraskevopoulou, C., et al., 2017. Time-dependent behaviour of brittle rocks based on static load laboratory tests. Geotech. Geol. Eng. 36 (1), 337–376.

Peng, J., Rong, G., Cai, M., Zhou, C.-B., 2015. A model for characterizing crack closure effect of rocks. Eng. Geol. 189, 48–57.

Pijnenburg, R., Verberne, B., Hangx, S., Spiers, C., 2018. Deformation behavior of sandstones from the seismogenic Groningen gas field: role of inelastic versus elastic mechanisms. J. Geophys. Res. Solid Earth 123 (7), 5532–5558.

Pijnenburg, R.P.J., Spiers, C.J., 2020. Microphysics of inelastic deformation in reservoir sandstones from the seismogenic center of the groningen gas field. Rock Mech. Rock Eng. 53 (12), 5301–5328.

Pijnenburg, R.P.J., Verberne, B.A., Hangx, S.J.T., Spiers, C.J., 2019. Inelastic deformation of the slochteren sandstone: stress-strain relations and implications for induced seismicity in the groningen gas field. J. Geophys. Res. Solid Earth 124 (5), 5254–5282.

Ranalli, G., 1995. Rheology of the Earth. Springer Science & Business Media.

Raziperchikolaee, S., Alvarado, V., Yin, S., 2022. Assessment of permeability changes during rock deformation and failure of a sandstone sample using a stress-dependent pore network model. Geomech. Geophys. Geo-Energy Geo-Res. 8 (2).

Reitenbach, V., Ganzer, L., Albrecht, D., Hagemann, B., 2015. Influence of added hydrogen on underground gas storage: a review of key issues. Environ. Earth Sci. 73, 6927–6937.

Sabitova, A., et al., 2021. Experimental compaction and dilation of porous rocks during triaxial creep and stress relaxation. Rock Mech. Rock Eng. 54 (11), 5781–5805.

Serra-Aguila, A., Puigoriol-Forcada, J., Reyes, G., Menacho, J., 2019. Viscoelastic models revisited: characteristics and interconversion formulas for generalized Kelvin–Voigt and Maxwell models. Acta Mech. Sin. 35, 1191–1209.

Tiab, D., Donaldson, E.C., 2024. Petrophysics: Theory and Practice of Measuring Reservoir Rock and Fluid Transport Properties. Elsevier.

Tullis, J., 1983. Deformation of feldspars. Feldspar Mineral. 2, 297–323.

Tullis, J., Yund, R., 1992. The brittle-ductile transition in feldspar aggregates: an experimental study. International Geophysics. Elsevier, pp. 89–117.

Vajdova, V., Baud, P., Wong, T.f., 2004. Permeability evolution during localized deformation in Bentheim sandstone. J. Geophys. Res. Solid Earth 109 (B10).

Wang, H., Xu, W., Cai, M., Xiang, Z., Kong, Q., 2017. Gas permeability and porosity evolution of a porous sandstone under repeated loading and unloading conditions. Rock Mech. Rock Eng. 50, 2071–2083.

Wang, Q., Hao, S., 2023. Creep behavior and permeability evolution of red sandstone in three Gorges Reservoir area subjected to cyclic seepage pressure. Geomech. Energy Environ. 36.

Wang, Q., et al., 2023. Terrestrial dominance of organic carbon in an Early Cretaceous syn-rift lake and its correlation with depositional sequences and paleoclimate. Sediment. Geol. 455, 106472.

Wang, Q., Li, Y., Sanei, H., Gardner, J., Rudra, A., Utley, J.E.P., et al., 2025. Lacustrine and fan-delta sediments in syn-rift lake basins. Deposit. Rec. 00, 1–36.

Wang, R., Li, L., 2018. Burgers creep model used for describing and predicting the creep behaviour of a rock under uniaxial and triaxial compression test conditions. Proceedings of the 71st Canadian Geotechnical Conference. Canadian Geotechnical Society, Edmonton.

Wei, E., et al., 2022. Nonlinear viscoelastic-plastic creep model of rock based on fractional calculus. Adv. Civ. Eng. 2022 (1), 3063972.

Wong, T.-f., Baud, P., 2012. The brittle-ductile transition in porous rock: a review. J. Struct. Geol. 44, 25–53.

Wong, T.-f., Brace, W., 1979. Thermal expansion of rocks: some measurements at high pressure. Tectonophysics 57 (2–4), 95–117.

Wong, T.f., David, C., Zhu, W., 1997. The transition from brittle faulting to cataclastic flow in porous sandstones: mechanical deformation. J. Geophys. Res. Solid Earth 102 (B2), 3009–3025.

Wu, F., et al., 2020. Long-term strength determination and nonlinear creep damage constitutive model of salt rock based on multistage creep test: implications for underground natural gas storage in salt cavern. Energy Sci. Eng. 8 (5), 1592–1603.

Wu, X., Liu, Z., 2022. Advances in deformation and permeability evolution during creep of rocks. Geotechnics 2 (2), 317–334.

Yang, S.-Q., Hu, B., 2018. Creep and long-term permeability of a red sandstone subjected to cyclic loading after thermal treatments. Rock Mech. Rock Eng. 51 (10), 2981–3004.

Zhang, J., Wong, T.F., Davis, D.M., 1990. Micromechanics of pressure-induced grain crushing in porous rocks. J. Geophys. Res. Solid Earth 95 (B1), 341–352.

Zhang, S., Wu, S., Zhang, G., 2020. Strength and deformability of a low-porosity sandstone under true triaxial compression conditions. Int. J. Rock Mech. Min. Sci. 127, 104204.

Zhang, Y., Shao, J., Xu, W., Jia, Y., 2016. Time-dependent behavior of cataclastic rocks in a multi-loading triaxial creep test. Rock Mech. Rock Eng. 49 (9), 3793–3803.

Zhang, Z.-H., Tang, C.-A., 2020. A novel method for determining the crack closure stress of brittle rocks subjected to compression. Rock Mech. Rock Eng. 53 (9), 4279–4287.

Zhao, Y., Wang, Y., Wang, W., Wan, W., Tang, J., 2017. Modeling of non-linear rheological behavior of hard rock using triaxial rheological experiment. Int. J. Rock Mech. Min. Sci. 93, 66–75.

Zheng, H., Feng, X.-T., Hao, X.-J., 2015. A creep model for weakly consolidated porous sandstone including volumetric creep. Int. J. Rock Mech. Min. Sci. 78, 99–107.

Zhong, C., Zhang, Z., Ranjith, P.G., Zhang, C., Xue, K., 2021. The role of pore pressure on the mechanical behavior of coal under undrained cyclic triaxial loading. Rock Mech. Rock Eng. 55 (3), 1375–1392.

Zimmerman, R.W., 1990. Compressibility of sandstones.

Zivar, D., Kumar, S., Foroozesh, J., 2021. Underground hydrogen storage: a comprehensive review. Int. J. Hydrogen Energy 46 (45), 23436–23462.

Zoback, M.D., 2010. Reservoir Geomechanics. Cambridge university press.